Universidad de Concepción

FACULTAD DE CIENCIAS FÍSICAS Y MATEMÁTICAS
DOCTORADO EN CIENCIAS FÍSICAS

Experimentos Usando Qudits de Camino en Altas Dimensiones para Información Cuántica

(Experiments Using High Dimensional Path Qudits for Quantum Information)

Advisor: Dr. Gustavo Moreira Lima
Departamento de Física
Facultad de Ciencias Físicas y Matemáticas
Universidad de Concepción

Submitted this thesis in partial fulfillment of the requirements for the degree of Doctor

Daniel Martínez Arias

Concepción, Chile
September 2019

Examiners: Dr. Gustavo Moreira Lima
Dr. Esteban Sepúlveda Gómez
Dr. Gustavo Cañas Cardona

Para mi amada esposa Fabita,
por su incondicional amor, cariño y paciencia

Contents

Contents vii

List of Figures ix

List of Tables xii

Acknowledgments xiii

Abstract xvii

Resumen xix

1 Introduction 1

2 Theoretical background 3
- 2.1 High dimensional quantum states 3
- 2.2 Dimensional witness 4
- 2.3 Communication Complexity Problems 5
- 2.4 Quantum state tomography 6

3 Experimental setup description 9

3.1 Experimental setup 9
3.2 Amplitude and phase characterization 11
3.3 Mean number of photons μ measurement 12
3.4 Electronic control system 14

4 Certifying an irreducible 1024-dimensional photonic state using refined dimension witnesses 17
4.1 Introduction 17
4.2 Gamut dimension witness 18
4.3 Experiment 22
4.4 Conclusion 26

5 High-dimensional quantum communication complexity beyond strategies based on Bell's theorem 27
5.1 Introduction 27
5.2 The communication complexity problems 28
5.3 The efficiency of quantum communication 31
5.4 Experimental demonstration of high-dimensional quantum communication advantage 33
5.5 Conclusion 37

6 Experimental quantum tomography assisted by multiply symmetric states in higher dimensions 39
6.1 Introduction 39
6.2 Theory 40
6.3 Experiment 50
6.4 Concluding remarks 55

7 Conclusion 61

8 Conclusión 63

Bibliography 65

List of Figures

3.1 Experimental setup. 10

3.2 Spatial Light Modulator with seven slits. 11

3.3 Normalized number of counts vs GL for SLM3 and SLM4. 12

3.4 Relative phase between the slits vs GL. One of the slits has a GL = 0 and the other is variable. 13

3.5 Counts in the detector and calculated probabilities for $\mu = 0.87$. 14

3.6 Top module diagram containing the most representative modules in the control system, working on a Xilinx Spartan6 FPGA. 15

4.1 Our d-dimensional QRACs scenario. Alice receives the input dits x_1 and $x_2 \in \{1, \dots, d\}$, and prepares the state $\rho_{x_1 x_2}$ which is sent to Bob. He receives the input $y \in \{1, 2\}$, which defines the quantum measurement M^y and the classical post-processing function $\mathcal{D}^y$ to be applied to $\rho_{x_1 x_2}$. As a result, Bob outputs b. 19

4.2 **a**. Experimental setup. We employ a prepare-and-measure scheme to generate and project spatial qudits, encoded into the linear transverse momentum of single-photons. At the state preparation block, the spatial encoding is applied through two spatial light modulators (SLMs), and the state projection is likewise performed by a SLM combined with a point-like single-photon detector (APD) at the measurement projection block (see main text for details). **b**. The 32×32-square mask addressed by the SLMs. 23

4.3 Experimental results. We experimentally observe $\bar{p} = 0.515 \pm 0.008$, violating the second highest ASP bound $\bar{p}_{Q_{512} \otimes Q_2}$ (see Tab.4.1). The error bar is calculated assuming Poissonian statistics for a photon detection event. 25

5.1 (a) Quantum CCP implementation based on the violation of the CGLMP inequalities. (b) Quantum CCP implementation based on communicating a single d-level quantum system. 30

5.2 Experimental setup for implementing the CCPs with quantum communication. d-dimensional quantum systems are encoded into the linear transverse momentum of single photons. The experiment is composed of two main parts: one for the state preparation and another for performing measurements on the prepared system. Both parts rely on the programmability of spatial light modulators for preparing the required states and measurements. 34

5.3 Experimental results. Δ_d^{Exp} is represented by red points. The yellow points represent Δ_d^{Bell}. The blue points are the theoretical predictions of Δ_d^{QS}. The green points represent Δ_d^{ML}. 36

6.1 Left panels: Condition number $\mathcal{C}\left(\mathcal{G}(\alpha)\right)$ as function of α—given that fiducial state $|\alpha_0\rangle$ is given by Eqs. (6.24) and (6.25)—for dimensions 6 and 15. Red squares indicate the values of α that were used in the experiment reported in this article. Since $\mathcal{C}\left(\mathcal{G}(\alpha)\right)$ might adopt very different values, these graphs were presented in logarithmic scale. Right panels: Fidelity of reconstructed states simulated by Monte Carlo method. 47

6.2 Experimental setup. 51

6.3 Examples of the Monte Carlo simulations performed (uppper panels) and their respective histograms (lower panels). Three horizontal dot-dashed lines in the upper graphs represent the mean value ($\langle F \rangle$) of the simulations and the $\langle F \rangle \pm 5\sigma$ interval. The continuous line in each histogram represents a fitted beta distribution. For each fitted function, the probability of having a value outside the $\pm 5\sigma$ interval is $\sim 10^{-6}$. . . . 54
6.4 Reconstructed quantum states for $D = 6$. The insets show the theoretically expected results. 56
6.5 Reconstructed quantum states for $D = 15$. The insets show the theoretically expected results. 57

List of Tables

4.1 Relevant cases for a 1024-dimensional system and the respective optimal ASPs (Eq.(4.1)) considering each product structure. 21

5.1 Lower bounds for the maximal value of Δ_d^{QS} as compared to the maximal value of Δ_d^{Bell} obtained via the maximal quantum (and macroscopically local i.e., Δ_d^{ML}) violation of the CGLMP inequalities. The final column was obtained through optimization over unit-trace measurement operators and optimal measurements were always found to be rank-one projective. 32

6.1 Values of K_s depending on the values of s and dimension, where $\boldsymbol{\kappa} = [\![D/2]\!]$. 42
6.2 Values of α chosen for experimental purposes. Numbers in parentheses below each α indicate the condition number, which is extracted from data of Figure 6.1. 50
6.3 Fidelities obtained for each of the reconstructed states, with their respective 5σ uncertainty extracted from 10000 Monte Carlo trials. MLE was used in each trial. 58

Acknowledgments

The PhD has been a tremendous adventure to me. I had the opportunity to meet very kind people that I'd like to thank.

First of all, I thank and recognize the work of my PhD advisor, Gustavo Lima, because he gave me the chance to work in his group even when he didn't meet me before. Even at those moments when I'm not feeling confident enough to be a serious scientist, Gustavo always have trust in me and he's continuously encouraging me to continue progressing during this years. Thanks for all the support Gustavo!

I want to thank specially to Gustavo Cañas. Since I arrived to Concepción, Gustavo helped me in many ways, but maybe what I mostly appreciate from him is the patience he has with me, his teachings and all the discussions in the lab. Thank you Gustavo for all the hand-to-hand work.

Many things I have learnt from my friends in UdeC, so I thank to Santiago, Miguel, Johanna, Esteban, Aldo, Guix, Pablo, Felipe, Álvaro, Tania, Nayda, Ítalo, Giannini, Mauricio and Matías. I also thank to Jaime Cariñe fo his friendship and the support on FPGA, C# and electronics he gave me. This is an amazing group and I'm truly grated to work with you guys!

After every endlessly and tired day there has been two smiling faces waitng for me at home: Fabi and Juli. I love you girls and I thank for your tender love. I'd like to thank my family in México for their inconditional love, for their daily calls and the support they gave me every day. This accomplishment couldn't had been without you. And my main thank is to God for this bless in my life and for the wisdom He gives us at every step in our lifes.

Abstract

In this dissertation an experimental method to generate and measure high dimensional quantum states is presented. Weak coherent pulses in the single photon level are prepared when a continuous wave 690 nm laser is pulsed with an Acousto Optical Modulator (AOM) and attenuated using neutral filters. The quantum states are encoded in the transverse linear momentum (TLM) of individual photons. The manipulation of TLM is performed by Spatial Light Modulators (SLMs), who display sets of d transmissive apertures (slits) giving the photon d alternative paths to propagate through, addressing the d dimensional state $|\psi\rangle$ the user wants to prepare. Two SLMs combined manipulate the real and imaginary part of the coefficients of $|\psi\rangle$, completing the generation stage of the setup. The SLMs are fully automated using Field Programmable Gate Array (FPGA) electronics. Once the state is generated, we can choose a previously calculated projective measurement $\langle\phi|$ to be implemented. This is done preparing a new set of d slits in another pair of SLMs, located in the measurement stage of the setup. Finally, an Avalanche Photo Diode masked with a 10 μm pinhole measures the overlap probability of $|\langle\phi\psi\rangle|^2$ from the accumulated statistics of the binary APD outcomes. Since the visibility of the output signal of the is around 0.98, a wide variety of quantum tasks can be performed using the presented experimental setup.

Resumen

En esta disertación se presenta un método para generar y realizar mediciones de estados cuánticos en altas dimensiones. Pulsos débilmente coherentes al nivel de fotones individuales son generados cuando un láser continuo es pulsado usando un AOM y atenuado con filtros neutros. Los estados cuánticos están codificados en el TLM de los fotones individuales. SLMs son usados para manipular el TLM cuando los SLM programan d aperturas transmisivas (rendijas), permitiendo que el fotón tenga d caminos posibles para su propagación, generando el estado d dimensional $|\psi\rangle$ que el usuario desea. Los SLMs están completamente automatizados mediante electrónica basada en FPGA. Una vez que el estado es generado, escogemos una medida proyectiva (previamente calculada) $\langle\phi|$ que es implementada al preparar un nuevo conjunto de d rendijas en los SLMs localizados en la etapa de medición del experimento. Finalmente, un Fotodiodo de Avalancha (APD) mide la probabilidad de $|\langle\phi\psi\rangle|^2$ al acumular la estadistística necesaria a partir de las medidas binarias que el APD proporciona. Debido a que la visibilidad del las salidas de nuestro experimento es de 0.98, una amplia variedad de tareas cuánticas pueden ser realizadas usando el arreglo experimental presentado.

CHAPTER 1

Introduction

During the last years, Quantum Computing (QC) and Quantum Information (QI) has become a relevant matter under the eyes of the scientific community and also for business companies. Several protocols and ideas for cryptography, tomography, error corrections, communication, fundamental physics, and many others had been proposed and proved, making this field a promising framework for the development of new technologies [94, 178]. Nevertheless, QC and QI is still in its dawn, it's said that we are living an age similar to the 60's, when the transistor/computer science had its initial steps. The development of QC and QI protocols and the experimental implementation of them are crucial steps in order to lead mankind to the quantum technology era.

In this dissertation we explore the experimental generation of high dimensional quantum states using TLM of single photons. We propose that TLM is an excellent framework to work in high dimensional QI. Our reasons are based on the high visibility obtained in this method, since it is high enough to perform cutting edge protocols in the area. The construction of such experimental setup is economically affordable since commercial SLMs can be used for de manipulation of such states. SLMs are controlled by conventional video signals, that we generate using FPGA. Another advantage is the reprogrammability of SLMs, letting us to perform different consecutive generation and projections of quantum states, or even perform a new experiment just by changing the set of states and measurement basis stored in the FPGAs. Today, the use of SLMs for the generation of quantum states is a well established technique used by the QI community [172, 171, 34]. During my PhD I have been working on the realization and publication of three letters, whose are already published in prestigious journals, and we're still working in the production of one more. The list of the mentioned works is the following:

- Certifying an Irreducible 1024-Dimensional Photonic State Using Refined Dimension Witnesses. *Phys. Rev. Lett.*, 120(23):230503 [3].
- High-Dimensional Quantum Communication Complexity beyond Strategies Based on Bells Theorem. *Phys. Rev. Lett.*, 121(15):150504 [111].
- Experimental quantum tomography assisted by multiply symmetric states in higher dimensions. *Phys. Rev. A*, 99(012336) [110].
- High dimensional adaptive standard quantum tomography [136].

To end this chapter I present the outline of this dissertation. The second chapter covers the theoretical background needed for the description of the generated states, including basic notions of HD quantum states and QI definitions needed to understand the main experiments here presented. The third chapter explains with more detail the experimental setup. The fourth, fifth and sixth chapters are about the three experiments we published. The final chapter includes the conclusions and final remarks.

CHAPTER 2

Theoretical background

2.1 High dimensional quantum states

The generation, manipulation and measurement of high-dimensional quantum systems (qudits) are important theoretical and experimental research subjects in quantum information science. This is motivated, in part, because certain fundamental features of quantum mechanics such as, for instance, quantum contextuality [154, 89, 35], cannot be tested with 2-dimensional quantum systems. The use of high-dimensional quantum systems also leads to improvements in several entangled based quantum information protocols since, in this case, some Bell inequalities exhibit increased robustness against noise [87, 44], and tolerate lower detection efficiencies for closing the detection loophole [173]. Last, due to the larger amount of information that can be encoded in single qudits, the performance of several protocols in quantum communications [25, 29, 39, 53, 122, 5] and quantum computation [123, 97, 103, 67, 167] is enhanced when they are employed. Typically, photonic platforms are used as test experiments to study quantum information processing in higher dimensions because different degrees of freedom of single photons can be efficiently used to encode the qudits. For instance, one can resort to the orbital angular momentum [107, 96, 83, 48, 1], frequency [98, 19, 92], time bin [158], path [142], and the transverse position/momentum [121, 120] encoding methods.

2.2 Dimensional witness

The dimension d of physical systems is a fundamental property of any model, and its operational definition arguably reflects the evolution of physics itself. In quantum mechanics, it can be seen as a key resource for information processing since higher dimensional systems provide advantages in several protocols of quantum computation [94] and quantum communications [178]. In the field of quantum foundations, a recent proposal suggests that in order to understand and create macroscopic quantum states it will be necessary to take advantage of high-dimensional systems [68]. Therefore, it is natural to understand why there is an growing strive to coherently control quantum systems of large dimensions [49, 57, 66, 48, 17, 60, 91, 177, 115, 174, 15, 108, 59]. Nonetheless, such new technological advances require the simultaneous development of practical methods to certify that the sources are truly producing the required quantum states. In principle, one can rely on the process of quantum tomography [51, 52, 85, 165, 99, 100, 71], but this approach quickly becomes intractable in higher dimensions as at least d^2 measurements are required [176].

To address this problem, the concept of dimension witness (DW) was introduced. The original idea was based on the violation of a particular Bell inequality [28], but then extended to the more practical prepare-and-measure scenario [64]. In general, DWs are defined as linear functions of a few measurement outcome probabilities and have classical and quantum bounds defined for each considered dimension [49, 28, 64, 4, 78, 27, 20]. Thus, they allow for the device-independent certification of the minimum dimension required to describe a given physical system, and can also infer if it is properly described by a coherent superposition of logical states. Nevertheless, these tests do not provide information about the composition of the system, which is crucial for high-dimensional quantum information processing. This point has been recently investigated by W. Cong et al. [45], where they introduced the concept of an irreducible dimension witness (IDW) to certify the presence of an irreducible 4-dimensional system. Specifically, their IDW distinguishes if the observed data is created by one pair of entangled ququarts, or two pairs of entangled qubits measured under sequential adaptive operations and classical communication.

2.3 Communication Complexity Problems

Communication complexity problems (CCPs) are tasks in which distant parties hold local data, the collection of which is needed for a computation of their interest. To make the computation possible, the parties communicate with each other. However, the amount of communication is limited and therefore not all data can be sent. The CCP consist in parties adopting an efficient communication strategy which allows them to perform the desired computation with a probability as high as possible. Efficient use of quantitatively limited communication is a broadly relevant matter [93], which provides fundamental insights on physical limitations [21, 130].

The ability to process information depends on the choice of the physical system into which the information is encoded [95]. Consequently, quantum entities without a classical counterpart can be regarded as tools for quantum information processing. The most famous example is entanglement. In a quantum CCP, parties may share an entangled state on which they perform local measurements, generating strongly correlated data which violates a Bell inequality. That data can then be used to assist a classical communication strategy [30]. In fact, Bell inequalities have been systematically linked to CCPs [24, 31, 163], and their violation enables better-than-classical communication efficiencies [43, 32, 25, 23, 24, 56, 77, 143, 163].

Nevertheless, quantum theory presents also a second approach to CCPs: substituting classical communication with quantum communication. Such a substitution must ensure that no more than the allowed amount of classical information can be extracted from the quantum communication, i.e., that the constraints of the CCP are respected. Since the Holevo theorem [79] implies that no more information can be extracted from a quantum d-level system than from a classical d-level system, a valid quantum communication strategy may encode information in quantum states of a specified limited Hilbert space dimension, and subsequently extract it by a measurement. The ability of quantum communication to outperform classical constraints in CCPs is well-established [7, 6, 38, 65, 119, 169, 75, 159, 150].

Many quantum communication tasks can be successfully completed both by means of local measurements on an entangled state followed by classical communication, or by the communication of a single quantum system [55, 61, 180]. For two-party CCPs with binary communication followed by binary-outcome measurements, classical communication assisted by correlations violating a Bell inequality is always at least as good as an implementation based on quantum communication [131]. Explicit examples in which the advantage is strict are known [132, 76]. However, there also exists examples of particular scenarios of two-party CCPs with more than two outcomes in which quantum communication holds an advantage over the Bell inequality based approach [160, 161].

2.4 Quantum state tomography

Quantum tomography (QT) is a collection of methods that makes possible the estimation of unknown quantum states [128]. Today, QT has become a standard tool for the quality assessment of the generation of quantum states [22, 124], the implementation of quantum processes [41, 42, 114], and the performance of quantum devices [50, 166]. Quantum tomographic methods provide an estimate of the unknown state from the outcomes of measurements carried out on an ensemble of identically, independently prepared systems. Finite statistics effects and unavoidable experimental errors require the postprocessing of the experimentally acquired data by means of statistical inference methods such as, for instance, maximum likelihood estimation [81, 85, 84, 140] or bayesian inference [86, 149, 33, 144, 82, 90, 156, 72, 70]. Traditionally, the total number of measurement outcomes is considered as a resource. Thus, there is a search for QT methods relying on a smaller number of measurement outcomes [46, 74, 71, 133]. Standard quantum tomography for a single qudit is based on the measurement of a D-dimensional representation of the D^2-1 generators of the SU(D) group, which leads to a total number of measurement outcomes of $2D^2-D$ [165]. This number can be reduced to D^2+D with quantum tomography based on mutually unbiased bases (MUB) [176]. The existence of MUB has been proven when the dimension D is an integer power of a prime number [14, 54]. Otherwise, the existence of mutually unbiased bases is still an open problem. A further reduction can be achieved with quantum tomography based on a symmetric informationally complete (SIC) positive-operator valued measure (POVM), which consists of D^2 sub-normalized projectors [141]. This is the smallest number of measurement outcomes to estimate unknown quantum states. Numerical studies [146, 63, 73] have indicated the existence of this class of measurements in all dimensions up to $D = 1155$ and exact analytical solutions are available in dimensions $D = 216, 19, 24, 28, 35, 48, 120, 124,$ and 323 [146, 9, 11, 10, 12]. Unfortunately, a dimension-independent demonstration is still missing.

CHAPTER 3

Experimental setup description

During this chapter I will cover some fundamental aspects of the experimental setup. Then I will show the process to characterize the transmission and phase of the SLMs. Also I will discuss about the measurement of the mean photon number, an important factor taking into account that we want to work in the single photon regime. Finally, I will briefly cover the electronic control system and I will explain the distribution of the main program running in the FPGA.

3.1 Experimental setup

At the preparation stage we generate an state of a single qudit that is encoded in a single photon. A 690 nm continuous-wave laser, an AOM, and calibrated attenuators (not shown in figure 3.1 for sake of clarity), are employed to generate weak coherent pulses. These illuminate spatial light modulators SLM1 and SLM2, which with the help of polarizers (P) and quarter-wave plates (QWP) are employed to modulate the incoming light in amplitude and phase, correspondingly. Electronically addressable slits patterns at SLM1 (as shown in 3.2) and SLM2 control the state $|\psi^d\rangle$ of the photonic qudit, ash shown in equation 3.1. The measurement stage projects state $|\psi^d\rangle$ onto a predefined, arbitrary single-qudit state $|\phi_j\rangle$. Spatial light modulators SLM3 and SLM4, combined with a pointlike avalanche photodiode (APD), implement the projection. In this way we are able

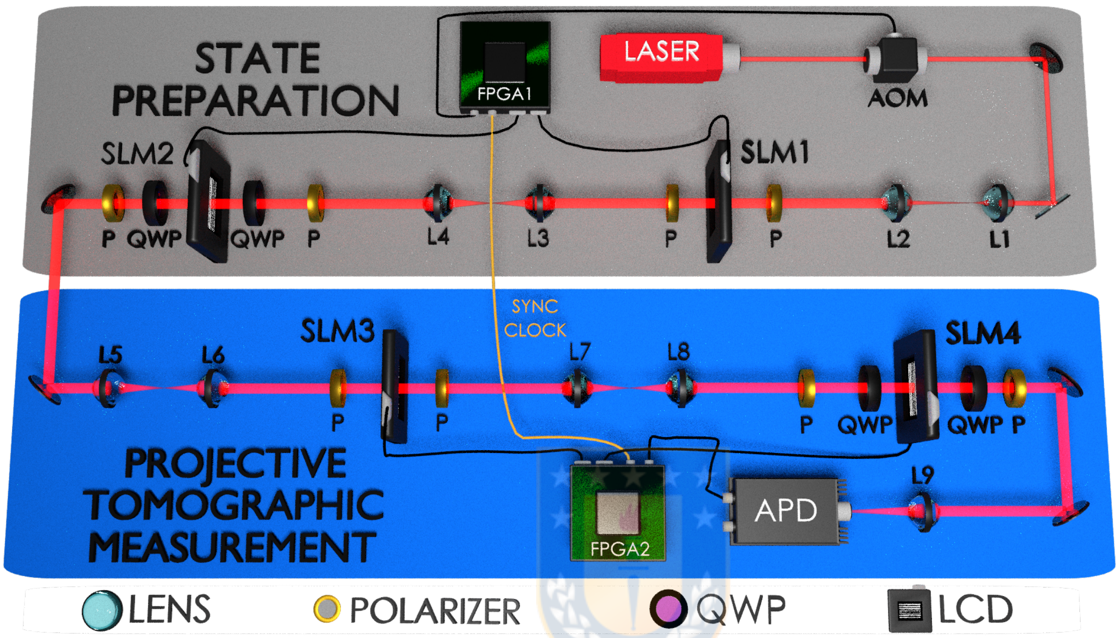
STATE PREPARATION
FPGA1
LASER
AOM
SLM2
SLM1
P
QWP
QWP
P
L4
L3
P
P
L2
L1
SYNC CLOCK
SLM3
SLM4
L5
L6
L7
L8
P
P
P
QWP
QWP
P
L9
APD
FPGA2
PROJECTIVE TOMOGRAPHIC MEASUREMENT
LENS
POLARIZER
QWP
LCD

Figure 3.1: Experimental setup.

to estimate the probability $|\langle\phi_j|\psi^d\rangle|^2$. A set of lenses is employed to transport the images generated by the SLMs along the setup. Focal lengths are as follows: L1 = 25 mm, L2 = 200 mm, L3=L4=L5=L6=L7=L8=125 mm, and L9 = 100 mm. The overall detection efficiency is around 13%.

$$|\psi\rangle = \frac{1}{\sqrt{d}} \sum_{l=-d/2}^{d/2} \sqrt{t_l} e^{i\phi_l} |l\rangle \tag{3.1}$$

$$|l\rangle = \sqrt{\frac{a}{\pi}} \int dq e^{-iqld} \sin qa |1, q\rangle$$

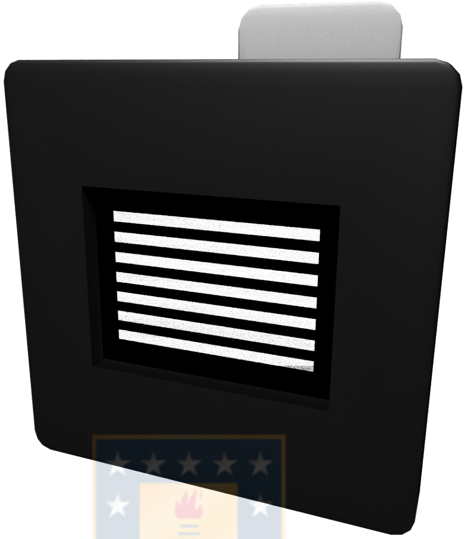

Figure 3.2: Spatial Light Modulator with seven slits.

3.2 Amplitude and phase characterization

The characterization of the transmittance and phase profiles of each SLM is a crucial requirement in order to program the exact gray level in the LCD and in this section I will describe the process and results of such characterizations.

Amplitude characterization

The basic idea is to display two slits in the LCD, with a fixed gray level, shine a light pulse for a fixed amount of time and measure the resulting counts using an Avalanche Photo diode placed in the center of the interference pattern in the Far Field plane of the last SLM. Then we repeat the process once again but this time changing the gray level value for both slits. The experiment is repeated for the 256 different gray level values (8 bit) and a histogram is plotted. Take as an example the figure 3.3, concerning to the amplitude characterization of SLM3 and SLM4.

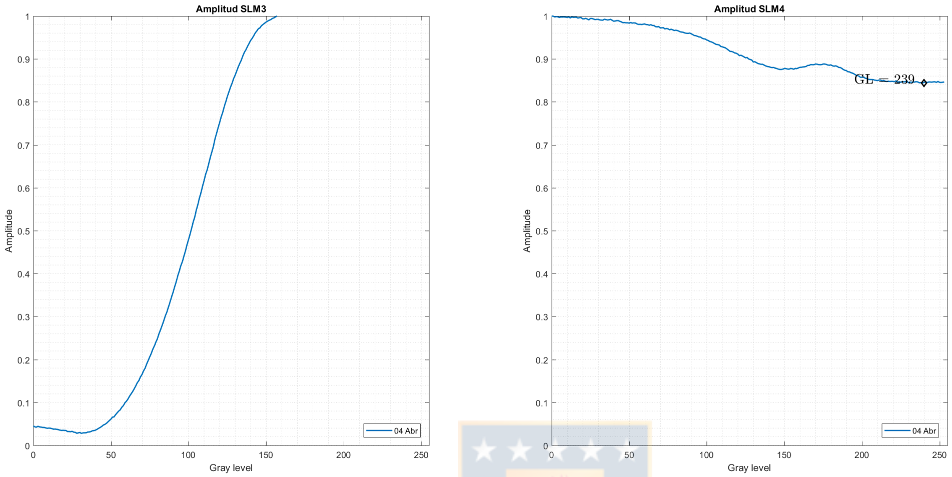

Figure 3.3: Normalized number of counts vs GL for SLM3 and SLM4.

Phase characterization

For this characterization we display two slits, we take a photo of the interference pattern in the far field plane of the SLM and finally a Matlab routine fits the pattern to a previously calculated one.

As discussed earlier, we display two slits, the first one has a fixed gray level value of 0 and the other slit changes its gray level value form pulse to pulse. Once we've taken the 256 photos and fitted all plots we can extract the relative phase between the the actual gray level value and zero. The figure 3.4 shows the phase characterization of SLM2 and SLM4.

3.3 Mean number of photons μ measurement

An approximation to a single photon source can be produced when we generate weak coherent pulses. Pulsing a continuous wave laser and a proper attenuation lead us to the single photon regime. Photons in such pulses follow the Poissonian

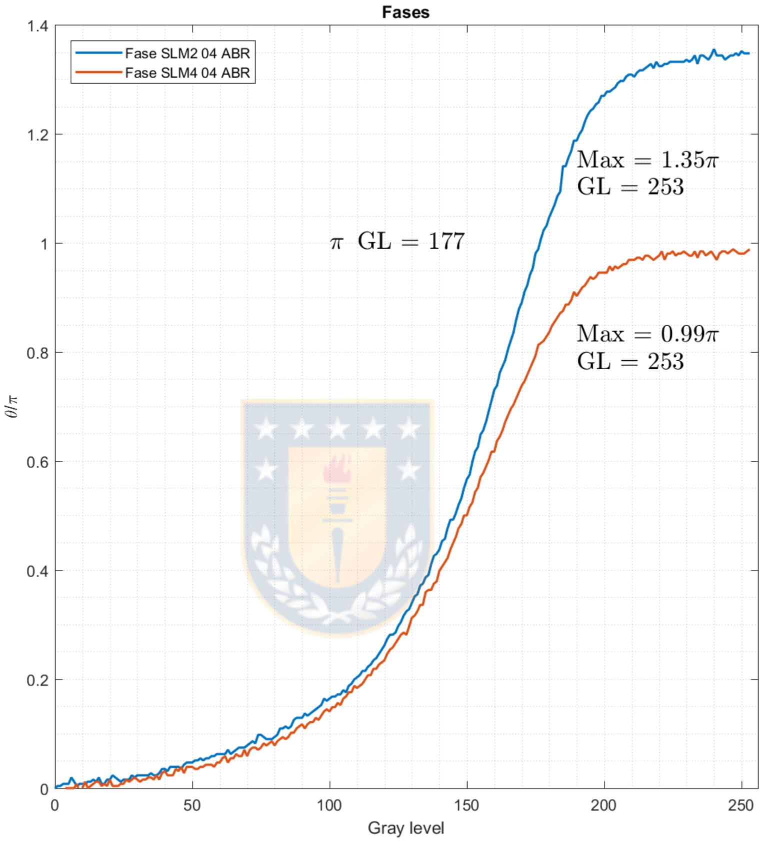

Figure 3.4: Relative phase between the slits vs GL. One of the slits has a GL = 0 and the other is variable.

distribution, that reads as follows

$$P(n|\mu) = \frac{\mu^n e^{-\mu}}{n!} \tag{3.2}$$

In order to measure μ we prepare the measurement $|\langle\psi|\psi\rangle|^2$ and record the number of counts in each pulse. In figure 3.5 we present an histogram of the number of pulses that have n clicks in the detector. Fitting the probabilities to the poissionan

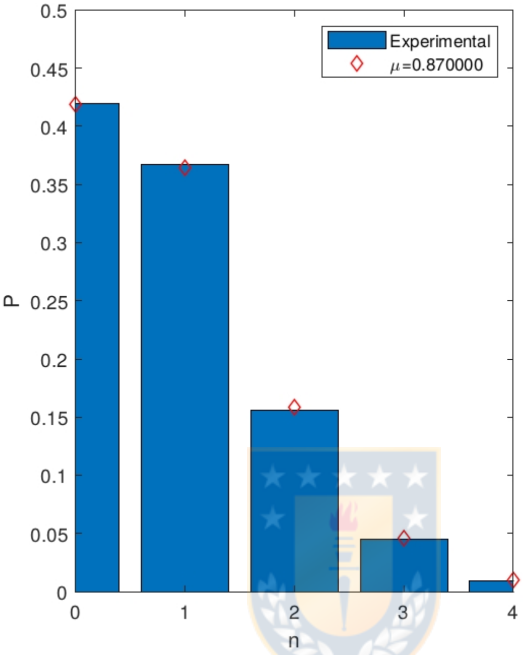

Figure 3.5: Counts in the detector and calculated probabilities for $\mu = 0.87$.

distribution we can find the appropriate experimental parameters involved in the generation of the pulse in the AOM.

3.4 Electronic control system

The control system of the experiment is based on FPGA electronics. We use the Atlys-Spartan6 FPGA from Xilinx, due to its versatility, port connections and speed. We use it control the light pulses, the HDMI video signals for the SLMs, the state and measurement vectors storage in a Random Access Memory (RAM) module, the Universal Asynchronous Receiver and Transceiver (UART) for the communication between FPGA and PC and finally a module for recording the clicks counted in the APD. I wrote all the programs in the *Verilog* language and also a Visual C# application for controlling the system. The system is user friendly and straight forward to use. The C# app needs the user to enter the states in a

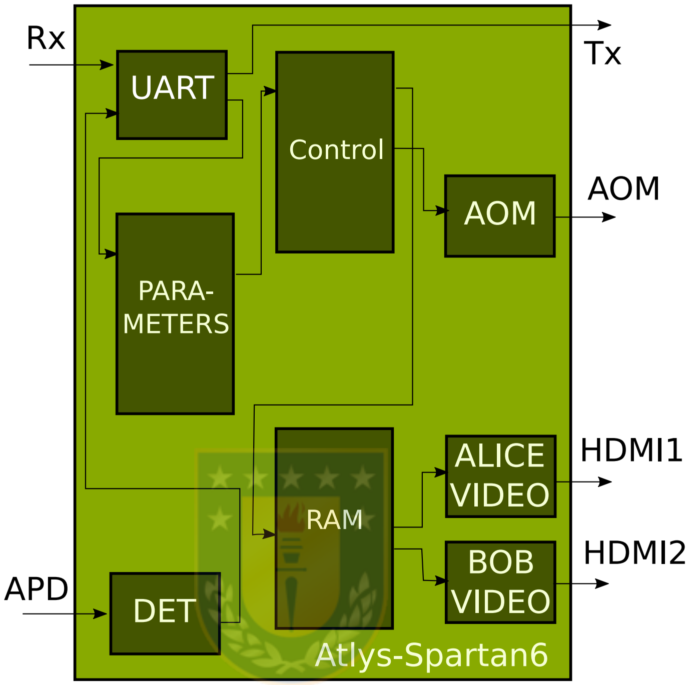
Rx
UART
Tx
Control
AOM
AOM
PARA-
METERS
HDMI1
ALICE
VIDEO
RAM
HDMI2
BOB
VIDEO
APD
DET
Atlys-Spartan6

Figure 3.6: Top module diagram containing the most representative modules in the control system, working on a Xilinx Spartan6 FPGA.

.txt file so they are sent and stored in the RAM module of the FPGA. By today, the system is fully automated, so it can work continuously for the days needed to complete the experiments. In figure 3.6 the block diagram of the main program is shown.

CHAPTER **4**

Certifying an irreducible 1024-dimensional photonic state using refined dimension witnesses

4.1 Introduction

In this experiment we introduce a new class of DWs, namely gamut DWs, which certifies the dimension of the system and has the new distinct feature of identifying whether any high-dimensional quantum system is irreducible. It is based on quantum random access codes (QRACs), which is a communication task defined in a prepare-and-measure scenario [8]. To demonstrate the practicability of our new technique we experimentally certify the generation of an irreducible 1024-dimensional photonic quantum system encoded onto the transverse momentum of single photons transmitted over programmable diffractive optical devices [57, 120, 99, 100, 71, 101, 37]. To our knowledge, our work represents an increase of about two orders of magnitude to any reported experiment using path qudits. From the recorded data one observes a violation of the bounds associated to all possible decompositions of a 1024-dimensional quantum system, thus, certifying that the generated state is not encoded using non-coupled different degrees of freedom of a photon, e.g., polarization and momentum. For instance, the ability to certify whether different non-coupled degrees of freedom of a single photon are simultaneously being used to encode information is crucial for the security of quantum communication tasks, as there could be information leakage that wont be detected in the communication protocol. Nonetheless, our method is broadly relevant and should also find applications in multipartite photonic scenarios and new platforms for the fast-growing field of experimental high-dimensional quantum information processing.

4.2 Gamut dimension witness

As stated earlier, the protocol we use in our main theorem is based on QRACs. Thus, we first give a brief description (see e.g. [8] for more details) of this task (see Fig. 4.1): one of the parties, Alice, receives two input dits: x_1 and $x_2 \in \{1, \ldots, d\}$. She is then allowed to send one d-dimensional (quantum) state, $\rho_{x_1 x_2}$ to Bob, depending on her input. Bob is then given a bit $y \in \{1, 2\}$ and his task is to guess x_y. He does so by performing a quantum measurement M^y and a classical post-processing function $\mathcal{D}^y$. As a result, he outputs $b \in \{1, \ldots, d\}$.

For a single round of the protocol, the success probability is $\mathbb{P}(b = x_y \mid x_1, x_2, y)$. As a figure or merit over many rounds with uniformly random inputs, we employ the *average success probability* (ASP): $\bar{p} = \frac{1}{2d^2} \sum_{x_1, x_2, y} \mathbb{P}(b = x_y \mid x_1, x_2, y)$. Thus, we are looking for the maximal value of $\bar{p}$, optimizing over all possible encoding and decoding strategies. It was proven [47] that for classical strategies (i.e. classical states and decoding functions), the optimal ASP is $\bar{p}_{C_d} = \frac{1}{2}(1 + \frac{1}{d})$. In the quantum case, the optimal strategy is reached by using mutually unbiased bases (MUBs) for encoding and decoding [2, 58], and the ASP is $\bar{p}_{Q_d} = \frac{1}{2}(1 + \frac{1}{\sqrt{d}})$.

Now, we estimate the optimal ASPs for composite systems, for all possible product structures, defined as follows:

Definition 4.2.1 *For a fixed d, we define a product structure by the set $\{r, \{d_k\}, \{\alpha_k\}\}$. For a composite system, $d = \prod_{k=1}^{r} d_k$, where d_k is the dimension of each subsystem and r is the number of subsystems. The state of the composite system can be written as $\rho = \rho^1_{\alpha_1} \otimes \rho^2_{\alpha_2} \otimes \cdots \otimes \rho^r_{\alpha_r}$. Here, $\alpha_k = c$ and $\alpha_k = q$ are used to denote the "classical" and "quantum" nature of the subsystem, respectively. Then, $\rho^k_c \in \Delta_{d_k - 1}$ is a classical state, and $\rho^k_q \in \mathcal{S}(\mathbb{C}^{d_k})$ is a quantum state.*

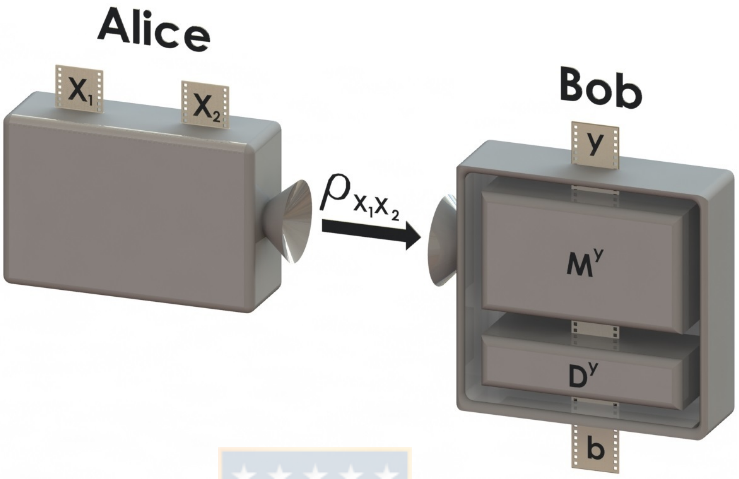

Figure 4.1: Our d-dimensional QRACs scenario. Alice receives the input dits x_1 and $x_2 \in \{1, \dots, d\}$, and prepares the state $\rho_{x_1x_2}$ which is sent to Bob. He receives the input $y \in \{1, 2\}$, which defines the quantum measurement M^y and the classical post-processing function $\mathcal{D}^y$ to be applied to $\rho_{x_1x_2}$. As a result, Bob outputs b.

Consider a set of measurement and state preparation settings, and fix the total dimension of the physical system in question. We call a linear function on the measurement outcome probabilities a gamut dimension witness (GDW), if its extremal values for all possible product structures are different. For example, in $d = 4$, a GDW has different extremal values for a ququart, two qubits, one qubit and a bit, and a quart. The main theoretical result of this work is to demonstrate that d-dimensional QRACs can be used as GDWs for d-dimensional physical systems. To highlight this, we set it as a theorem.

Theorem 1 *d-dimensional QRACs serve as gamut dimension witnesses using the ASP function.*

The proof of this theorem and all related lemmas can be found in the supplementary material of [3]. Let us now sketch the main tools for proving the theorem. They help to understanding the problem, and can be independently used. Note that the following lemmas apply in more general QRAC scenarios as well.

We assume that Bob's measurements have the same product structure as the state generated by Alice. That is, we exclude that Bob's state certification would use entangling measurements. The motivation here is to rule out sequential uses of lower dimensional systems as a way to simulate higher dimensional statistics, e.g. to discriminate between n sequential uses of a d dimensional system, and a d^n dimensional system. A physical motivation for this assumption is to think that if Alice cannot couple a particular set of degrees of freedom (e.g. polarization and momentum), then neither can Bob because he has access to the same equipment as Alice does.

Therefore, the most general strategy for decoding the d-dimensional system $\rho = \rho^1 \otimes \rho^2 \otimes \cdots \otimes \rho^r$ is as follows: Bob performs sequential adaptive measures on the subsystems in the sense of [45]. He starts by measuring subsystem ρ^1 to obtain the outcome b^1. Then, his choice of the measurement to be performed in ρ^2 may depend on b^1. Successively, each measurement on ρ^k can depend on all the measurement outcomes obtained previously. After performing all measurements, Bob feeds the obtained outcomes to a classical post-processing function, and outputs his final guess on x_y, which is $b = \mathcal{D}^y(b^1 b^2 \dots b^r)$.

The bounds of the GDW in this general scenario are extremely hard to obtain. The following results help making the analysis easier. First, it is argued in [8] that in an optimal strategy, it is enough to use encoded pure states. Similarly, it has been shown that rank 1 projective measurements (explicitly: mutually unbiased bases) optimize two-input QRACs [58]. Thus,in the following we only deal with pure states for both Alice and Bob. Additionally, we can eliminate classical post-processing functions:

Lemma 4.2.1 *In QRACs, for optimality of the ASP, there is no need for classical post-processing functions.*

Last, we note that:

Lemma 4.2.2 *In QRACs, for optimality of the ASP, there is no need for sequential adaptive measurements.*

Observe that the above lemmas together imply that the highest ASP for a composite system can be achieved with a strategy that consists of r QRACs *in parallel*, one on each subsystem ρ^k, independently. In this case, if we write Alice's inputs as dit-strings $x_y = x_y^1 x_y^2 \dots x_y^r$, the success probability for each round

Case	Optimal $\bar{p}$
Q_{1024}	0.515625
$Q_{512}Q_2$	0.500980
$Q_{512}C_2$	0.500973
$Q_{32}Q_{32}$	0.500521
$(Q_2)^{10}$	0.500493
Q_2C_{512}	0.500489
C_{1024}	0.500488

Table 4.1: Relevant cases for a 1024-dimensional system and the respective optimal ASPs (Eq.(4.1)) considering each product structure.

is: $\mathbb{P}(b = x_y|x_1, x_2, y) = \prod_{k=1}^{r} \mathbb{P}(b^k = x_y^k|x_1^k, x_2^k, y)$. The optimal $\bar{p}$ is not necessarily given by the independent optimal strategies on the individual subspaces. Therefore, in order to optimize it we introduce the *trade-off function* $\mathcal{M}_d(z)$, which provides the optimal probability of guessing dit x_2 given a fixed probability of guessing dit x_1. Let $z = \mathbb{P}(\text{Bob correctly guesses } x_1)$. Then, $\mathcal{M}_d(z)$ in dimension d is defined by $\mathcal{M}_d(z) = \max\{\mathbb{P}(\text{Bob correctly guesses } x_2)|z\}$, where the maximization is limited to all encoding-decoding strategies respecting the condition of guessing x_1 with probability z. Thus, in a general case

$$\bar{p}_{Q_{d_1}\dots C_{d_r}} = \max_{z^1,\dots,z^r} \frac{1}{2}[z^1 \cdots z^r + \mathcal{M}^q_{d_1}(z^1)\cdots\mathcal{M}^c_{d_r}(z^r)], \tag{4.1}$$

where we denote d-dimensional quantum and classical states by Q_d and C_d, respectively. $\mathcal{M}^q_d$ and $\mathcal{M}^c_d$ are the corresponding quantum, and classical trade-off functions . Therefore, $\bar{p}$ is a function of r real variables, and its maximum can be found using standard heuristic numerical search algorithms [139]. We present the ASP optimal values for some relevant cases of a $d = 1024$ dimensional system in Table 4.1. The full list of cases is found in the supplementary material [3]. Note that the gaps between the different ASP values are large enough to be experimentally observed, as we demonstrate next.

4.3 Experiment

To demonstrate the practicability of our technique we generate a 1024-dimensional photonic state, encoded into the linear transverse momentum of single-photons, and use the 1024-dimensional QRAC GDW to certify that it is an irreducible quantum system. To achieve this, we first show that the ASP (Eq.(4.1)) can be written as a simple function of the detection events. Then, we observe that our recorded statistics violate the second highest ASP bound, $Q_{512}Q_2$, given in Table 4.1. Thus, ensuring that it is an irreducible 1024-dimensional quantum system.

In the 1024-dimensional QRAC GDW, Bob measures the elements of the two 1024-dimensional MUBs given in the supplementary material [3]. We denote the MUBs states by $|m_j^y\rangle$, where $y = 1, 2$ defines the measuring base MUB_1 or base MUB_2, and $j = 1, ..., 1024$ denotes the state of a given base. Alice's state is written in terms of the two input dits x_1 and x_2 as an equal superposition of the states Bob would need to guess x_y correctly:

$$|\Psi_{x_1x_2}\rangle = \frac{1}{N}(|m^1_{x_1}\rangle + \mathrm{sgn}(\langle m^1_{x_1}|m^2_{x_2}\rangle)|m^2_{x_2}\rangle), \tag{4.2}$$

where $N = \sqrt{2(1+\frac{1}{32})}$ is a normalization factor and sgn is the sign function. The optimality of the encoded states (4.2), and the use of MUBs is derived in the supplementary material [3].

For the experimental test, we resort to the setup depicted in Fig. 4.2. At the state preparation block, the single-photon regime is achieved by heavily attenuating optical pulses with well calibrated attenuators. An acousto-optical modulator (AOM) placed at the output of a continuous-wave laser operating at 690nm is used to generate the optical pulses. The average number of photons per pulse is set to $\mu = 0.4$. In this case, the probability of having non-null pulses is $P(n \geqslant 1|\mu = 0.4) = 33\%$. Pulses containing only one photon are the majority of the non-null pulses generated and accounts to 82% of the experimental runs. Thus, our source is a good approximation to a non-deterministic single-photon source, which is commonly adopted in quantum communications [178].

The single-photons are then sent through two spatial light modulators, SLM1 and SLM2, addressing an array of 32×32 transmissive squares. The square side is $a = 96\mu\text{m}$ and they are equally separated by $\delta = 160\mu\text{m}$ (see Fig. 4.2b). Thus, effectively creating a 1024-dimensional quantum state defined in terms of the

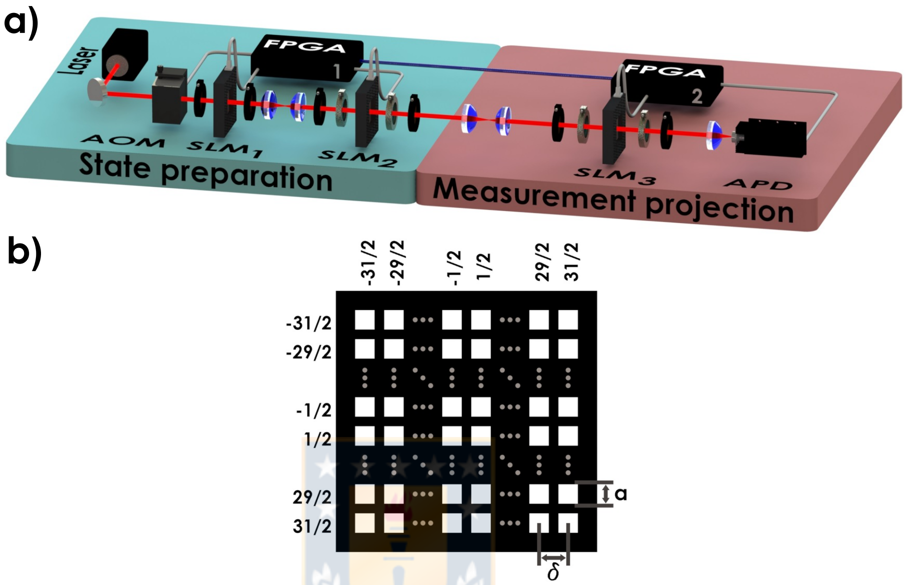

Figure 4.2: **a**. Experimental setup. We employ a prepare-and-measure scheme to generate and project spatial qudits, encoded into the linear transverse momentum of single-photons. At the state preparation block, the spatial encoding is applied through two spatial light modulators (SLMs), and the state projection is likewise performed by a SLM combined with a point-like single-photon detector (APD) at the measurement projection block (see main text for details). **b**. The 32×32-square mask addressed by the SLMs.

number of modes available for the photon transmission over the SLMs [57, 120, 99, 100, 71, 101]. Specifically, the state of the transmitted photon is given by $|\Psi\rangle = \frac{1}{\sqrt{C}}\sum_{l=-l_{N_c}}^{l_{N_c}}\sum_{\nu=-l_{N_r}}^{l_{N_r}}\sqrt{t_{l\nu}}e^{-i\phi_{l\nu}}|c_{l\nu}\rangle$, where $|c_{l\nu}\rangle$ is the logical state representing the photon transmitted by the (l,ν) square. $t_{l\nu}$ represents the transmission and $\phi_{l\nu}$ the phase-shift given by the (l,ν) square. The transmission of each square is controlled by the SLM1, which is configured for amplitude-only modulation. The phases $\phi_{l\nu}$ are controlled by SLM2 working on the configuration of phase-only modulation [100]. N_c and N_r represent the number of columns and rows, respectively. For simplicity, we define $l_{N_c} \equiv \frac{N_c-1}{2}$, $l_{N_r} \equiv \frac{N_r-1}{2}$, and C is the normalization factor.

At the measurement block we use a similar scheme to the one used in the state preparation block. It consists of a SLM3, also configured for phase-modulation, and a "pointlike" avalanche single-photon detector (APD). As explained in details at [100, 57], by placing the "pointlike" APD at the SLM3 far-field (FF) plane, and properly adjusting the (l, ν) square phase-shifts, Bob can detect any state $|m_j^y\rangle$ required for the 1024-dimensional QRAC session. The "pointlike" APD is composed of a pinhole (aperture of 10μm diameter) fixed at the center of the FF plane, followed by the APD module. In this case, the probability of photon detection is proportional to the overlap between the prepared and detected states. For the case of a d-dimensional QRACs implemented with a single-detector scheme, we show at the supplementary material that the ASP function can be written as [3]

$$\bar{p} = \frac{D_1}{D_1 + D_2}. \tag{4.3}$$

We first consider the events with $x_y = j$ (again, $j = 1, ..., 1024$ denotes the state of a given base) and define the total number of such events to be X_1. Then, we define D_1 as the number of "clicks" recorded in the experiment in those cases. Likewise, we denote X_2 to be the number of events where $x_y \neq j$ and define D_2 to be the clicks in those cases.

By means of two field-programmable gate arrays (FPGA) electronic modules we are able to automate and actively control both blocks of the setup. At the state preparation block, since the state $|\Psi\rangle$ needs to be randomly selected from the set of states defined by the 1024-dimensional QRACs, a random number generator (QRNG - Quantis) is connected to FPGA1. FPGA1 controls the optical pulse production rate by the AOM, set at 60 Hz as limited by the refresh rate of the SLMs. Each attenuated optical pulse corresponds to an experimental round. At the measurement block, a second QRNG is connected to FPGA2, providing an independent and random selection for the projection $|m_j^y\rangle$ at each round. FPGA2 also records whether a detection event occurs. The overall detection efficiency is 13%. The protocol is executed as follows: In each round, FPGA1 reads the dits x_1 and x_2 produced by its QRNG. Then, FPGA1 calculates the amplitude and phase of each (l, ν) square of SLM1 and SLM2 to encode the state $|\Psi_{x_1 x_2}\rangle$ onto the spatial profile of the single-photon in that experimental round. Simultaneously, FPGA2, reads from its QRNG the value of y and j. Similar to what is done in the state

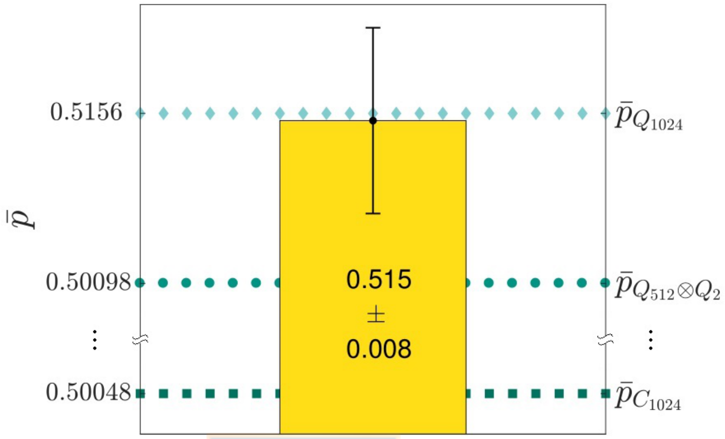

Figure 4.3: Experimental results. We experimentally observe $\bar{p} = 0.515 \pm 0.008$, violating the second highest ASP bound $\bar{p}_{Q_{512}\otimes Q_2}$ (see Tab.4.1). The error bar is calculated assuming Poissonian statistics for a photon detection event.

preparation block, FPGA2 also calculates the phase for each (l, ν) square in SLM3 to implement the chosen projection $|m_j^y\rangle$. The amplitude and relative phase for each SLM was previously characterized in order to obtain the modulation curves as a function of its grey level. In this experiment, this is necessary to dynamically generate all possible states, as it would be unfeasible to pre-record pre-defined masks for the SLMs on the FPGAs for each one of the 1024^2 required initial states.

The experiment continuously ran over 316 hours. In this way, the statistics fluctuations observed for D_1 and D_2 were sufficiently small to unambiguously certify the generation of an irreducible 1024-dimensional quantum system. The overall visibility in our system is $97.00 \pm 0.07\%$ and the corresponding recorded average success probability is $\bar{p} = 0.515 \pm 0.008$. In Fig. 4.3 we compare it with the second highest ASP bound shown in table 4.1, associated with a composite system of the type $Q_{512}Q_2$. This certifies, only from the statistics recorded, that the generated state is not encoded using non-coupled different degrees of freedom of a photon, for instance polarization and momentum. Thus, ensuring it to be an irreducible 1024-dimensional quantum system that can provide all the advantages known for high-dimensional quantum information processing, in the sense explained in [45].

4.4 Conclusion

Dimension witnesses are practical protocols on the field of quantum information as they allow one to obtain information regarding unknown quantum states [28, 64]. They are especially appealing while addressing the generation and characterization of high-dimensional quantum states, where quantum tomography demands at least d^2 measurements [176]. In general, DWs are functions of only a few measurement outcome probabilities and allow for assessments on the dimension required to describe a given quantum state in a device-independent way [49, 28, 64, 4, 78, 27, 20]. Here we give a step further by introducing a new class of DW, which certifies the dimension of the system, and has the new distinct feature of allowing the identification whether a high-dimensional system is irreducible. The application of this new feature is of broad relevance for several new architectures aiming for high-dimensional quantum information processing [49, 57, 66, 48, 17, 60, 91, 177, 115, 174, 15, 108, 59], and the understanding of macroscopic quantumness [68]. We demonstrate the practicability of our technique by using it to certify the generation of an irreducible 1024-dimensional photonic quantum state encoded into the linear transverse momentum of single-photons transmitted by programable diffractive apertures, which have been used for several high-dimensional quantum information processing tasks [57, 37, 109, 35, 152].

Chapter 5

High-dimensional quantum communication complexity beyond strategies based on Bell's theorem

5.1 Introduction

In this work, we theoretically explore and experimentally demonstrate advantages of performing CCPs with quantum communication in high-dimensional Hilbert space, as compared to exploiting the violation of a Bell inequality. To this end, we focus on a family of CCPs [25, 23] based on the (to the best of our knowledge) only known family of bipartite facet Bell inequalities. Facet inequalities optimally bound correlations with a local hidden variable model [26]. We consider the Collins-Gisin-Linden-Massar-Popescu (CGLMP) inequalities, involving any d number of outcomes [44, 112]. We demonstrate the advantage of quantum communication over strategies based on violations of the CGLMP inequalities, which we show to be even larger than previously thought [161]. In particular, whilst resolving two conjectures of [161], we show that below dimension six, both quantum CCP-implementations are equally efficient, whereas above (and including) dimension six they are not. In this sense, dimension six acts as a threshold for revealing the advantages of quantum communication. To shine light on the suddenly emerging discrepancy between the two quantum CCP-implementations, we evidence that optimal quantum communication strategies in high-dimensional Hilbert space require projective measurements that are not rank-one. Subsequently, we present an experimental realisation. Using high-dimensional photonic systems, specifically up to dimension ten, we outperform strategies based on violating the CGLMP inequalities, emerging from dimension six, by means of quantum nonlocal correlations. Furthermore, we also outperform strategies based on super-quantum violations of said inequalities respecting only no-signaling and macroscopic locality [118]. Finally, we prove that the experimental data cannot be simulated with any rank-one projective measurement without additional post-processing of the data. Since only a dimensional bound on the relevant Hilbert space is assumed, this constitutes a semi-device-independent [129] falsification of said property.

5.2 The communication complexity problems

Bell inequalities can be systematically mapped to CCPs. In a Bell experiment, any choice of shared state and local measurements, which then generates a probability distribution, can also be used in a strategy for a CCP leading to an efficiency analogous to that observed in the Bell experiment [24, 163]. A quantum advantage (in such strategies) over classical methods relies on generating correlations that violate the relevant Bell inequality. A natural candidate for such constructions are facet Bell inequalities, since these optimally bound correlations obeying local realism. The CGLMP inequalities [44] constitute a family of facet Bell inequalities for two parties, each with two choices of measurements and with $d \geqslant 2$ possible outcomes.

The construction of CCPs based on the CGLMP inequalities has been developed in [25, 23]. In this family of CCPs (parameterised by d), a party Alice is given random inputs $x_0 \in \{0, \ldots, d-1\}$ and $x \in \{0, 1\}$, and another party, Bob, is given a random input $y \in \{0, 1\}$. Alice may communicate no more than $\log d$ bits to Bob, after which he outputs a guess $g \in \{0, \ldots, d-1\}$. If g coincides with the value of a function $f_k(x_0, x, y) = x_0 - xy - (-1)^{x+y} k \mod d$, for some $k = 0, \ldots, \lfloor d/2 \rfloor - 1$, the partnership is awarded $c_k = 1 - 2k/(d-1)$ points. However, if g coincides with $h_k = x_0 - xy + (-1)^{x+y}(k+1) \mod d$, the partnership loses c_k points. The task is to efficiently communicate such that the average number of points earned is large. The payoff function is given by

$$\Delta_d^{\text{Bell}} = \frac{1}{4d} \sum_{\substack{x_0,x\\ y,k}} c_k \left[P(g=f_k|x_0,x,y) - P(g=h_k|x_0,x,y)\right].$$

On the one hand, in an approach based on Bell inequalities, Alice and Bob share an entangled state and perform local measurements x and y with d-valued outcomes a and b respectively. In order to exploit the fact that the CCP is tailored to the CGLMP inequalities, Alice encodes the classical communication $m(a,x_0,x) \in \{0,\ldots,d-1\}$ using $m = x_0 + a \mod d$ and Bob subsequently decodes it using $g = m - b \mod d$ (see Fig. 5.1). It was shown [25, 23, 161] that the resulting value of Δ_d^{Bell} is in one-to-one correspondence with the quantity evaluated from the statistics $p(a,b|x,y)$ in a test of the CGLMP inequalities. In this sense, the efficiency in the CCP is determined by the amount of nonlocality present in the distribution $p(a,b|x,y)$. In particular, if $p(a,b|x,y)$ generates a maximal violation of the (suitably normalised) CGLMP inequalities, then by the outlined communication strategy it can be used to achieve an equally large value of Δ_d^{Bell}. The maximal quantum value achievable in a test of the CGLMP inequalities lacks a simple analytical form but is known up to large d and achieved with non-maximally entanged states [179]. Violations of the CGLMP inequalities have been experimentally observed for high-dimensional systems [164, 48, 102].

On the other hand, these CCPs can also be implemented without exploiting entanglement and Bell inequality violations [161]. Instead, Alice and Bob can use single quantum systems for direct quantum communication. In such an implementation, Alice associates her random inputs (x,x_0) to a d-dimensional quantum state, $\rho_{x_0x} \in \mathbb{C}^d$, which is sent to Bob who performs a measurement $\{M_y^g\}_{g=0}^{d-1}$, the outcome g of which determines his output guess (see Fig. 5.1). In a quantum model, the performance of the CCP reads

$$\Delta_d^{\text{QS}} = \frac{1}{4d} \sum_{x_0,x,y,k} c_k \operatorname{tr}\left(\rho_{x_0x}\left(M_y^{f_k} - M_y^{h_k}\right)\right). \tag{5.1}$$

An efficient quantum communication strategy, i.e., a suitable choice of state preparations and measurements, aims to find the largest value of Δ_d^{QS}. In Supplementary Material we qualitatively discuss the advantages and limitations of the two

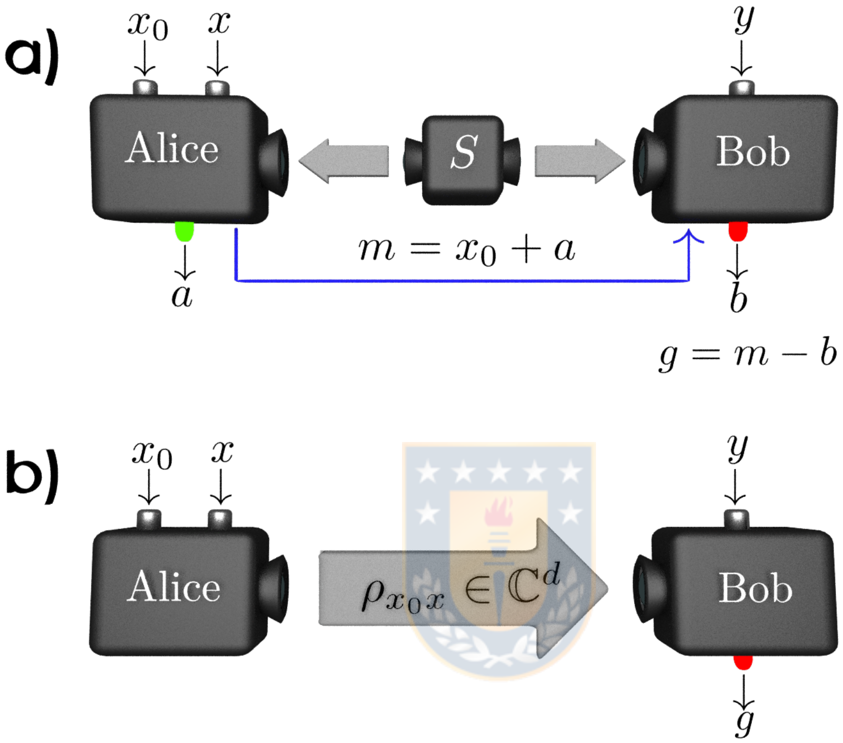

Figure 5.1: (a) Quantum CCP implementation based on the violation of the CGLMP inequalities. (b) Quantum CCP implementation based on communicating a single d-level quantum system.

quantum CCP implementations. In Ref. [161], it was shown that the optimal performance of the two different quantum approaches is equal, i.e., $\Delta_{\mathrm{d}}^{\mathrm{QS}} = \Delta_{\mathrm{d}}^{\mathrm{Bell}}$, when $\mathrm{d} = 2, 3, 4$. Numerical results suggested the same relation also for $\mathrm{d} = 5, 6$. However, for $\mathrm{d} \geqslant 7$, lower bounds on $\Delta_{\mathrm{d}}^{\mathrm{QS}}$ were shown to outperform the maximal value of $\Delta_{\mathrm{d}}^{\mathrm{Bell}}$. Next, we revisit this analysis, show improved quantitative results, establish the precise dimension revealing the inequivalence, and provide insight to the qualitative differences between the two quantum implementations of the CCPs.

5.3 The efficiency of quantum communication

We begin by quantifying the advantage of quantum communication over strategies based on the violation of the CGLMP inequalities. Specifically, we numerically infer lower bounds on the maximal value of Δ_{d}^{QS} for $d \leqslant 10$. This has been done by running two optimisations in see-saw [175, 127]; first optimising over the states of Alice for fix measurements of Bob, and then over the measurements of Bob for fix states of Alice, repeatedly. Each such optimization constitutes a semidefinite program [170]. The best found states and measurements are listed in Supplementary Material. The results are presented in Table 5.1 together with the known [179, 161] optimal CGLMP-based values of $\Delta_{d}^{\mathrm{Bell}}$ as obtained both in quantum theory, and by the super-quantum principle of macroscopic locality [118]. The latter correlations are only constrained by the inability of violating a Bell inequality when the measurements are macroscopic, i.e., that a large number of particles are collectively measured instead of microscopic measurements on single particles. The results substantially improve on the lower bounds for Δ_{d}^{QS} obtained in [161], and thus establish an increased quantitative advantage of high-dimensional quantum communication over strategies based on Bell inequality violation. In particular, note that for $d = 8, 9, 10$, quantum communication can even outperform the Bell inequality based approach when the correlations established are only required to be macroscopically local, i.e., the violation of the CGLMP inequalities is larger-than-quantum.

Furthermore, we rectify the main result of [161] by resolving two of its conjectures: that the optimal quantum communication strategy performs equally well as that based on the quantum violation of the CGLMP inequalities when $d = 5$ and when $d = 6$. For $d = 5$, we have used the second hierarchy level of dimensionally bounded quantum correlations [117]. In order to reduce the computational requirements of this evaluation, we have employed the symmetrisation techniques and toolbox of [162]. We obtain a tight bound on the efficiency of quantum communication matching that obtained through a maximal violation of the CGLMP inequalities. This proves the conjecture. For $d = 6$, the presented lower bound on Δ_{d}^{QS} shows that quantum communication outperforms the analogous Bell inequality based result. Thus, the improved lower bound falsifies the conjecture. This establishes dimension six as the dimension revealing the quantitative inequivalence between the two quantum implementations of the CCPs.

d	Lower bound Δ_d^{QS}	Lower bound Δ_d^{QS} from [161]	Δ_d^{Bell}	Δ_d^{ML}	Lower boundΔ_d^{QS} rank-one projective
2	-	0.7071	0.7071	0.7071	0.7071
3	-	0.7287	0.7287	0.7887	0.7287
4	-	0.7432	0.7432	0.8032	0.7432
5	-	0.7539	0.7539	0.8249	0.7539
6	0.8000	0.7624	0.7624	0.8345	0.7624
7	0.8175	0.7815	0.7694	0.8461	0.7814
8	0.8571	0.8006	0.7753	0.8529	0.8006
9	0.8622	0.8622	0.7804	0.8605	0.8188
10	0.8889	0.8778	0.7849	0.8657	0.8396

Table 5.1: Lower bounds for the maximal value of Δ_d^{QS} as compared to the maximal value of Δ_d^{Bell} obtained via the maximal quantum (and macroscopically local i.e., Δ_d^{ML}) violation of the CGLMP inequalities. The final column was obtained through optimization over unit-trace measurement operators and optimal measurements were always found to be rank-one projective.

A relevant question is whether the breaking of the equivalence of the two quantum implementations, emerging when the dimension is increased above five, is linked to qualitatively different properties in the optimal use of the respective quantum systems. Below the critical dimension six, the optimal found preparations of Alice can be effectively prepared by Alice locally measuring an entangled state, and then considering the post-measurement state of Bob for her given outcome. The collection of Bob's post-measurement states is then identical to the collection of states communicated over a quantum channel in an optimal strategy. Consequently, there is no advantage over Bell inequality based strategies. Furthermore, the optimal measurements coincide with the rank-one projective measurements optimal for violating the CGLMP inequalities. However, when $d \geqslant 6$ our numerical calculations for $d = 6, \ldots, 10$ suggests that: (I) the states $\{\rho_{x_0 x}\}$ cannot be prepared remotely with entanglement in a test of the CGLMP inequalities, and that some inputs may be associated to the same state, and (II) the two measurements of Bob are such that one is rank-one projective, whereas the other is higher-rank projective, i.e., some measurement operators are zero-operators, meaning that the associated outcomes never can occur regardless of the state being measured. Degenerate measurements are known to be optimal for some quantum information problems [126, 104]. They can be viewed as rank-one projective measurements with additional post-processing by which some outcomes remain untouched and other outcomes are given new labels. To further evidence the sub-optimality of rank-one projective measurements (without post-processing), we have numerically optimised Δ_d^{QS} over measurements in which all measurement operators are of trace one. Since all rank-one projectors are of trace one, and we always find the optimal measurement to be rank-one projective, the results constitutes a lower bound valid for such measurements. The results (see Table 5.1) show that although rank-one projective measurements are sufficient to outperform strategies based violating the CGLMP inequalities, they are not optimal.

5.4 Experimental demonstration of high-dimensional quantum communication advantage

We present an experimental demonstration of the advantages of single-system quantum communication in the considered CCPs for $d = 6, ..., 10$. In our experiment, d-dimensional quantum systems are encoded into the linear transverse momentum of single photons transmitted by programmable diffractive apertures, which nowadays is a standard technique used for high-dimensional quantum information processing [101, 100, 71, 36, 3, 155, 152, 109, 113, 105, 49, 62, 37].

The experimental setup is presented in Fig. 5.2. It is composed of two main parts: one for the state preparation and another for performing projective measurements on the prepared system. Each part is controlled by a Field Programmable Gate Array (FPGA) electronics. In the state preparation, a 690 nm single mode laser modulated with an Acousto-Optic Modulator (AOM) and optical attenuators (not shown in Fig. 5.2) prepare weak coherent states with an average number of 0.9 photons per pulse. This source can be seen as an approximation to a nondeterministic single-photon source, since pulses with a single-photon account for 62.3% of the generated non-null pulses. Accidental counts are strongly suppressed by using a detection window that matches the optical pulse duration of 45μs.

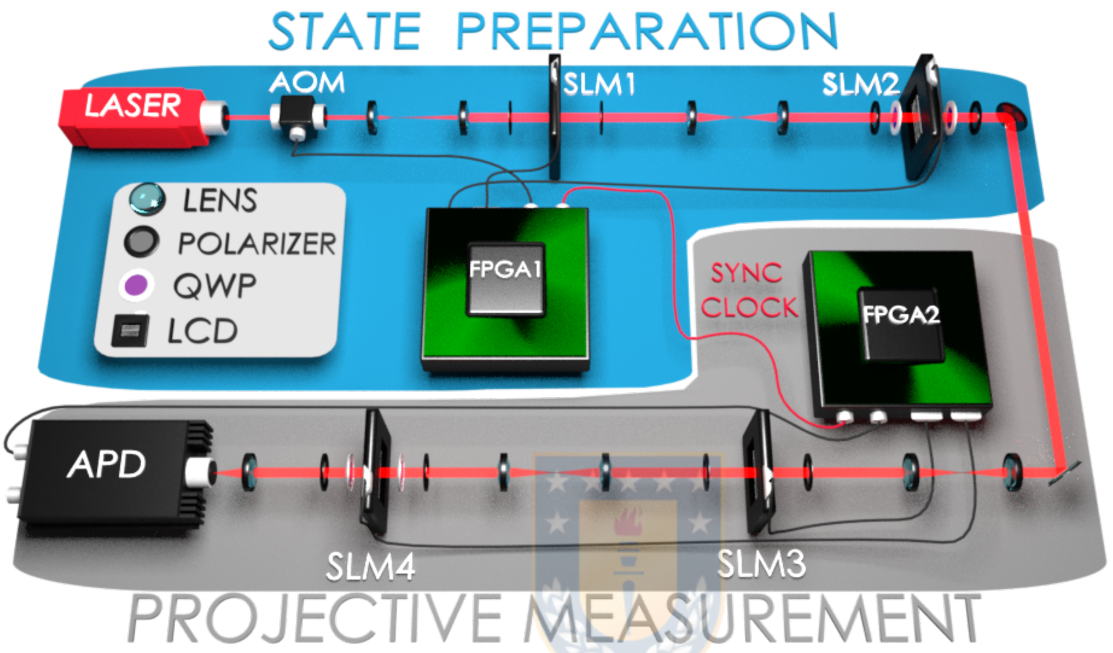

Figure 5.2: Experimental setup for implementing the CCPs with quantum communication. d-dimensional quantum systems are encoded into the linear transverse momentum of single photons. The experiment is composed of two main parts: one for the state preparation and another for performing measurements on the prepared system. Both parts rely on the programmability of spatial light modulators for preparing the required states and measurements.

To encode the quantum states in the linear transverse momentum of single photons we exploit the pixel-programmability of spatial light modulators (SLMs) [101, 100]. The state preparation and measurement stages has two fundamental blocks: an amplitude-modulation only SLM1 (SLM3), built with two linear polarizers and a liquid crystal display (LCD), and a phase-modulation only SLM2 (SLM4), composed of two linear polarizers, two quarter wave plates and an LCD. Each SLM is placed in the image plane of its predecessor. In order to experimentally generate some desired states $\rho_{x_0x} = |\psi_{x,x_0}\rangle\langle\psi_{x,x_0}|$, a set of d slits with a width of 64 μm and equal center to center separation are displayed on SLM1 and SLM2. The individual transmittances t_l and phases ϕ_l of each slit "l" are set to reconstruct the real and imaginary parts of $|\psi_{x,x_0}\rangle$. The state vector of the transmitted photon after the SLM2 is given by $|\psi\rangle = \frac{1}{\sqrt{N}} \sum_{l=-d/2}^{d/2} \sqrt{t_l} e^{i\phi_l} |l\rangle$, where N is a normalisation constant. The coefficients t_l and the phases ϕ_l are independently controlled by the SLM 1 and SLM 2, respectively. To implement the desired measurements at the measurement stage, different amplitude and phase sets of the d slits are used at the SLM3 and SLM4. The transmittances and phases of each set are chosen to post-select for detection one of the required state vectors $|\varphi_{y,b_y}\rangle$. In the final part of the setup, a "pointlike" avalanche single-photon detector (APD) with a 10 μm pinhole is placed at the center of the far field plane of the SLM4. In this case, the probability of single-photon detection $P(x, x_0, y, b)$ is proportional to $|\langle \varphi_{y,b} | \psi_{x,x_0} \rangle|^2$ [100, 71, 36, 3]. However, since for each d one of the targeted protocol measurements is rank-two projective (see Supplementary Material, we post-process the experimental data to emulate the statistics such a measurement. This is done by suitably relabling the outcomes of the relevant measurements whenever, in the raw data, it is associated to an outcome which never occurs in the desired rank-two projective measurement.

After several rounds of the experiment, an experimental value of Δ_d^{QS} is calculated from the acquired data, namely Δ_d^{Exp}. Since the measurement uncertainty of Δ_d^{Exp} decreases with the total number of counts, the repetition of the experimental rounds for each dimension were chosen such that Δ_d^{Exp} violates the bounds for Bell inequality based strategies with at least six standard deviations for each d considered. Hence, any explanation in terms of an arbitrary entangled quantum system is excluded by at least 6 standard deviations, which corresponds to a p-value of 1×10^{-9}.

For $d = 6, ..., 10$, we obtain the results

$$\begin{aligned} \Delta_6^{Exp} &= 0.7893 \pm 0.0026 & \Delta_7^{Exp} &= 0.8082 \pm 0.0034 \\ \Delta_8^{Exp} &= 0.8453 \pm 0.0041 & \Delta_9^{Exp} &= 0.8427 \pm 0.0051 \\ \Delta_{10}^{Exp} &= 0.8773 \pm 0.0018. \end{aligned} \tag{5.2}$$

In Figure 5.3, we compare the experimental results to the theoretical predictions for quantum communication, as well as with the limitations of both quantum and macroscopically local Bell correlations. The results are in good agreement with the theoretical predictions, surpassing the values associated to the maximal violation

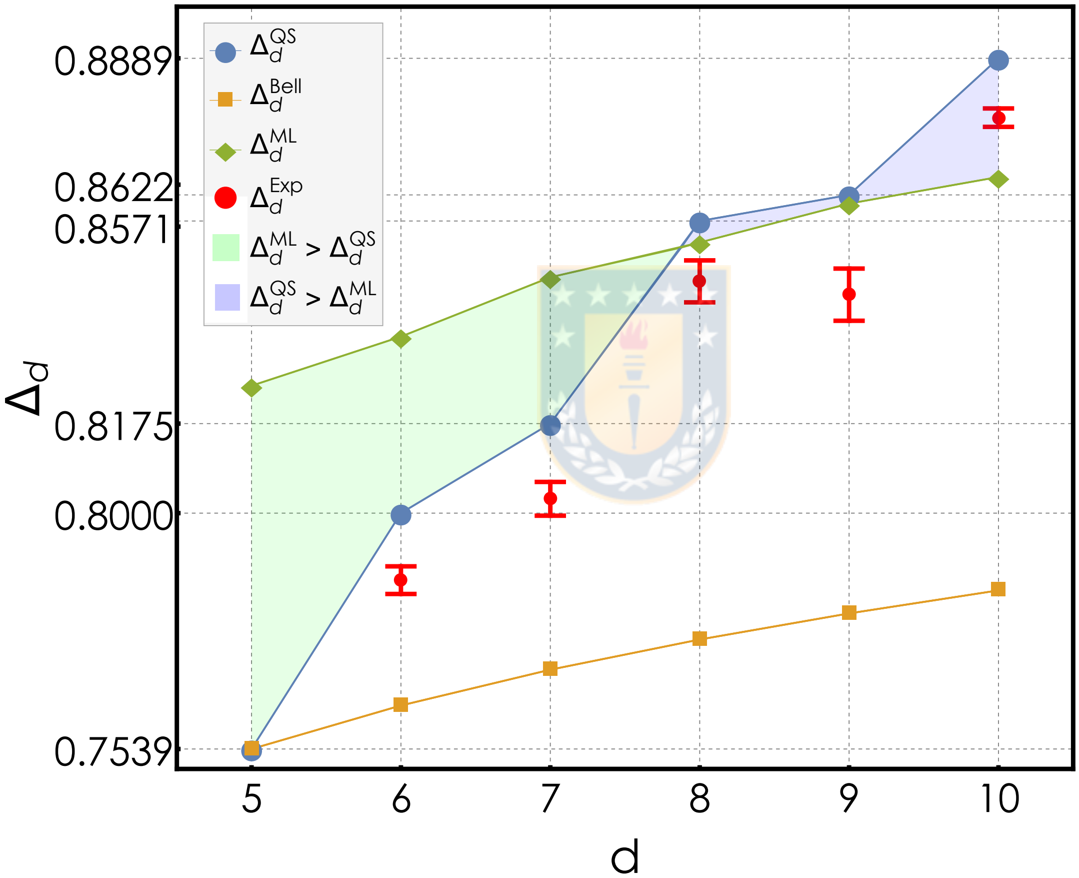

Figure 5.3: Experimental results. Δ_d^{Exp} is represented by red points. The yellow points represent Δ_d^{Bell}. The blue points are the theoretical predictions of Δ_d^{QS}. The green points represent Δ_d^{ML}.

of the CGLMP inequalities. In the particular, in the case of $d = 10$, the results also surpass the limitations of the post-quantum Bell correlations obeying only macroscopic locality.

Finally, we revisit the previously numerically evidenced hypothesis of rank-one projective measurements being sub-optimal. Focusing on the case of $d = 6$, we have considered whether the experimental data can be reproduced by some quantum communication strategy utilising only such measurements. To this end, we have used an intermediate level of the hierarchy of dimensionally bounded quantum correlations [117], and additionally imposed upper and lower bounds on the particular probabilities measured in the lab corresponding to $(x_0, x) = (4, 0)$ and $y = 0$. In order to respect the errors of the measured probabilities, they was constrained to an interval twice larger than the experimental errors of each measurement outcome. In this manner, we have obtained the bound 0.7830 on Δ_6^{QS} which is smaller than the experimentally measured value. This demonstrates that under the assumption of a six dimensional Hilbert space, there exists no quantum communication strategy based on rank-one projective measurements which can reproduce the experimental results.

5.5 Conclusion

We have theoretically and experimentally studied the efficiency of high-dimensional quantum communication in a family of CCPs, as opposed to classical communication assisted by nonlocal correlations violating the facet Bell inequality to which the CCPs were originally tailored. We demonstrated significant advantages of quantum communication which increase with Hilbert space dimension, and showed that they stem from degenerate measurements. Our work shows the usefulness and strength of quantum correlations generated via the communication of a high-dimensional quantum system, and the practicality of experimentally realising them.

CHAPTER 6

Experimental quantum tomography assisted by multiply symmetric states in higher dimensions

6.1 Introduction

In this experiment, we propose and experimentally test a new quantum tomographic method, which is based on the measurement of an informationally complete POVM formed by sub-normalized projectors onto multiply symmetric states [125]. These are constructed by applying products of integer powers of unitary transformations on a fixed fiducial quantum pure state. Unlike SIC-POVM and MUB, our tomographic method can be constructed in any finite dimension. Furthermore, in the case of odd dimensions, the POVM has D^2 sub-normalized projectors and thus it requires the smallest number of measurement outcomes to estimate unknown quantum states. In the case of even dimensions, the POVM has $3D^2/2$ measurement operators, which is a significative reduction from the case of standard tomography. A first estimate of the unknown state can be obtained by linear inversion, which does not introduce bias [145]. The numerical stability of this process can be improved at a great extent by a suitable choice of the fiducial state.

This also contributes to speed up the rate of convergence in the postprocessing of the experimentally acquired data. Our experimental implementation is based on the encoding of D-dimensional quantum states onto the linear transverse momentum of single photons. These are created by defining D different propagation paths available for the photon transmission at diffractive apertures addressed on spatial light modulators (SLM) [101]. A second set of SLMs allows one to project the D-dimensional state onto any other fixed D-dimensional state [100]. The use of SLMs for preparation [101, 100, 153, 172, 171] and measurement of these so-called spatial qudits has been extensively explored for quantum information tasks such as QKD [57], Bell-type nonlocality and noncontextuality tests [48, 35, 13, 34], and quantum tomography [137, 100, 138, 71], among others [152, 3, 111]. We test our tomographic method in dimensions 6 and 15 reaching fidelities of 0.998 and 0.984 with ensemble sizes of only 6×10^4 and 1.5×10^5, respectively. Experiments performed with similar optical setups have achieved lower fidelities of 0.96 for dimensions 6 and 7, 0.985 for dimension 8, and 0.887 for dimension 10 [100, 18, 71] while resorting to larger ensembles of detected photons. Thus, our experimental results demonstrate the practicability of our method in higher dimensions and the good performance of our experimental setup.

This article is organized as follows: In Sec. 6.2, we introduce the theoretical background and formulate our tomographic method. In Sec. 6.3, we introduce the experimental setup and analyze the results provided by the experimental realization of our method. In Sec. 6.4, we summarize, comment on possible extensions to the multipartite case, and conclude.

6.2 Theory

In this section we briefly recall the general notion of multiply symmetric states. Thereafter, we study a particular family of multiply symmetric states and build the tomographic method upon it. We solve explicitly the inversion problem and provide a simple analytical expression relating the experimentally acquired data, the measurement settings, and the estimate of the unknown state.

Multiply symmetric states

In general, states $|\psi_{k_1,k_2,\ldots,k_M}\rangle$ are said to be multiply symmetric if they can be written as [16]

$$|\psi_{k_1,k_2,\ldots,k_M}\rangle = U_1^{k_1} U_2^{k_2} \cdots U_M^{k_M} |\psi_{0,0,\ldots,0}\rangle, \tag{6.1}$$

where $k_j = 0, \ldots, N_j - 1$, $|\psi_{0,0,\ldots,0}\rangle$ is the fiducial state of the set, and U_j are unitary transformations that satisfy $U_j^{N_j} = \mathbb{I}$ (for every j), where $\mathbb{I}$ is the identity operator acting onto the Hilbert space of a single qudit. We will limit ourselves to the case of $M = 3$. Thus, we define the constant matrices

$$\mathcal{X} = \sum_{k=0}^{D-1} |k \oplus 1\rangle\langle k|, \tag{6.2}$$

$$\mathcal{Z} = \sum_{k=0}^{D-1} e^{2\pi i k/D} |k\rangle\langle k|, \tag{6.3}$$

$$\mathcal{V} = \sum_{k=0}^{\kappa-1} |k\rangle\langle k| - i \sum_{k=\kappa}^{D-1} |k\rangle\langle k|, \tag{6.4}$$

where D is the dimension of the Hilbert space and $\kappa = [\![D/2]\!]$, being $[\![x]\!]$ the operation that rounds x to the closest integer number. These matrices represent, respectively, the shift operator ($\mathcal{X}$), the clock operator ($\mathcal{Z}$) and an additional phase-only transform ($\mathcal{V}$) with diagonal entries $v_k = \langle k|\mathcal{V}|k\rangle$ that adopt values of 1 and $-i$. The symbol $\oplus$ in Eq. (6.2) denotes addition mod(D). By using the operators $\mathcal{X}$, $\mathcal{Z}$, and $\mathcal{V}$, we now define a set of multiply symmetric states $\{|\alpha_{\ell,m,j}\rangle\}$ given by

$$|\alpha_{\ell,m,j}\rangle = \mathcal{V}^{\ell} \mathcal{X}^{m} \mathcal{Z}^{j} |\alpha_0\rangle = \sum_{k=0}^{D-1} a_k v_{k\oplus m}^{\ell} e^{2\pi i jk/D} |k \oplus m\rangle, \tag{6.5}$$

where $\ell = 0, 1, 2, 3$, $m = 0, \ldots, D-1$, and $j = 0, \ldots, D-1$. The fiducial state is a pure quantum state $|\alpha_0\rangle = \sum_{k=0}^{D-1} a_k |k\rangle$, whose coefficients fulfill the normalization condition $\sum_{k=0}^{D-1} |a_k|^2 = 1$.

Value of s	K_s odd dimension	K_s even dimension
$0 \leqslant s \leqslant \kappa - 1$	D	$2D$
$\kappa \leqslant s \leqslant D - 1$	D	D
$D \leqslant s \leqslant D - 1 + \kappa$	Does not apply	$2D$

Table 6.1: Values of K_s depending on the values of s and dimension, where $\kappa = [\![D/2]\!]$.

Essential subsets of states

Let us now consider a physical system described by an unknown D-dimensional quantum state ρ. In 2010, Paiva-Sanchez and coworkers [125] studied quantum state tomography assisted by a basis $\mathcal{B}_0(\alpha)$ of D equidistant states, which they denoted as $|\alpha_j\rangle$. These states are such that the inner product between them is given by $\langle \alpha_j | \alpha_{j'} \rangle = \alpha$ $(j > j')$, where α is a fixed constant. Additional $D - 1$ bases $\mathcal{B}_s(\alpha)$ are constructed by applying $\mathcal{X}^s$ on the elements of $\mathcal{B}_0(\alpha)$. This amounts for a total of D^2 measurements. Additionally, they report a strange behavior that depends on the dimension of the Hilbert space where the state belongs to. In summary, odd dimensions require the aforementioned D^2 measurements only, whereas even dimensions require additional measurements attainable by applying $\mathcal{V}$ on the elements of each $\mathcal{B}_s(\alpha)$, which leads to a total of $3D^2/2$ measurements.

The form of the equidistant states used in Ref. [125] for this purpose resembles the one of Eq. (6.5). Nevertheless, an analysis of the computations of Ref. [125] indicates that a similar mathematical procedure allows us to accomplish such tomographic process regardless of the fiducial state used, that is, states $|\alpha_j\rangle$ do not need to be equidistant. Thus, we resorted to multiply symmetric states for such goal. If D is an odd number, quantum state tomography can be performed by measuring on projectors of the form $|\alpha_{0,m,j}\rangle\langle\alpha_{0,m,j}|$, with $\ell = 0$ and for every m and j ranging from 0 to $D - 1$. For even dimensions, we must also consider $\ell = 1$, with $j = 0, \ldots, D - 1$ and $m = 0, \ldots, D/2 - 1$ for these additional measurements.

In this context, a simpler mathematical description can be obtained by resorting to two subscripts only, regardless of the dimension. Thus, we define

$$\begin{aligned} |\alpha_{sj}\rangle &= \mathcal{V}^{\lfloor s/D \rfloor}\mathcal{X}^s\mathcal{Z}^j|\alpha_0\rangle, \\ &= \sum_{k=0}^{D-1} a_k v^{(s)}_{k\oplus s} e^{2\pi ijk/D}|k\oplus s\rangle, \end{aligned} \tag{6.6}$$

where $v^{(s)}_k = \langle k|\mathcal{V}^{\lfloor s/D \rfloor}|k\rangle$, $j = 0, \ldots, D-1$, $s = 0, \ldots, s_{\max}-1$, and

$$s_{\max} = \begin{cases} D, & \text{if D is odd,} \\ \dfrac{3D}{2}, & \text{if D is even.} \end{cases} \tag{6.7}$$

Thus, the set of states $\{|\alpha_{sj}\rangle\}$ in odd dimensions is still a complete set of multiply symmetric states under transformations $\mathcal{X}$ and $\mathcal{Z}$, as seen from Eq. (6.5). For even dimensions, on the other hand, this set encompasses a *subset* of the multiply symmetric states under the action of $\mathcal{X}$, $\mathcal{Z}$, and $\mathcal{V}$. Despite the different behavior exhibited by states $|\alpha_{sj}\rangle$ as defined here, they allow one to construct POVMs. Indeed, we may define

$$\Pi_{sj} = \frac{1}{K_s}|\alpha_{sj}\rangle\langle\alpha_{sj}|, \qquad \sum_{s=0}^{s_{\max}-1}\sum_{j=0}^{D-1}\Pi_{sj} = \mathbb{I}, \tag{6.8}$$

where the values of K_s are given in Table 6.1. This POVM will be useful for tomographic and post-processing purposes.

Tomography using multiply symmetric states

Let us define the matrix $\mathcal{P} = \sum_{s,j} p_{sj}|s\rangle\langle j|$, where $p_{sj} = \mathrm{tr}(\rho\Pi_{sj})$. Explicitly,

$$\begin{aligned} \mathcal{P} = \sum_{s=0}^{s_{\max}-1}\sum_{j=0}^{D-1}\Bigg(\sum_{l,m=0}^{D-1}\frac{a_l^* a_m}{K_s}e^{2\pi i(m-l)j/D} \\ \times v^{(s)*}_{l\oplus s}v^{(s)}_{m\oplus s}\rho_{l\oplus s,m\oplus s}\Bigg)|s\rangle\langle j|. \end{aligned} \tag{6.9}$$

This matrix contains the experimental probabilities that can be found by taking the completeness relation of Eq. (6.8) into consideration. So, if n_{sj} is the number of registered counts when Π_{sj} is measured, then every probability can be experimentally estimated as $p_{sj} = n_{sj}/\sum_{t,k} n_{tk}$. Afterwards, a right-Fourier transformed probability matrix $\widetilde{\mathcal{P}}$ can be defined as $\mathcal{P}\cdot\mathcal{F}$, where $\mathcal{F} = \frac{1}{\sqrt{D}}\sum_{l,m=0}^{D-1} e^{2\pi i l m/D}|l\rangle\langle m|$. Explicitly,

$$\begin{aligned}\widetilde{\mathcal{P}} = \sum_{k=0}^{D-1}\Bigg[&\sum_{s=0}^{s_{\max}-1}\frac{\sqrt{D}}{K_s}|s\rangle\\ &\times\left(\sum_{q=0}^{D-1} a^{*}_{q\ominus s\oplus k}\, a_{q\ominus s}\, v^{(s)*}_{q\oplus k}\, v^{(s)}_{q}\langle q|\right)|\vec{\rho}_k\rangle\Bigg]\langle k|,\end{aligned} \tag{6.10}$$

where $|\vec{\rho}_m\rangle$ denotes the m-th diagonal of ρ, given by[1]

$$|\vec{\rho}_m\rangle = \sum_{q=0}^{D-1}\rho_{q\oplus m,q}|q\rangle. \tag{6.11}$$

For convenience, we will define ancillary vectors

$$|\vec{\xi}_{sk}\rangle = \left(\mathcal{X}^{s-k}|\alpha_0\rangle\right)\circ\left(\mathcal{X}^{s}|\alpha_0\rangle^{*}\right)\circ\left(\mathcal{X}^{-k}|\vec{v}_s\rangle\right)\circ|\vec{v}_s\rangle^{*}, \tag{6.12}$$

where "$\circ$" denotes the Hadamard product between matrices, and

$$|\vec{v}_s\rangle = \sum_{r=0}^{D-1} v_r^{(s)}|r\rangle = \mathrm{diag}\left(\mathcal{V}^{\lfloor s/D\rfloor}\right). \tag{6.13}$$

Consequently, the right-transformed probability matrix can be compactly written as

$$\widetilde{\mathcal{P}} = \sum_{k=0}^{D-1}\mathscr{G}_k|\vec{\rho}_k\rangle\langle k|, \tag{6.14}$$

---

[1] Throughout this document, notation $|\vec{\alpha}\rangle$ will refer to a purely mathematical vector $\vec{\alpha}$ that does not represent any physical state. However, Dirac notation is used for comfortability.

where matrix $\mathscr{G}_k$ is given by

$$\mathscr{G}_k = \sum_{s=0}^{s_{\max}-1} \frac{\sqrt{D}}{K_s} |s\rangle\langle\vec{\boldsymbol{\xi}}_{sk}|. \tag{6.15}$$

Now, it is possible to construct the density operator ρ by rearranging its components in a vector $\vec{\rho} = \mathrm{vec}(\rho)$ (see Appendix of [110]), which is computed according to

$$\vec{\boldsymbol{\Delta}}_\rho = \sum_{k=0}^{D-1} |k\rangle \otimes |\vec{\boldsymbol{\rho}}_k\rangle, \tag{6.16}$$

$$\vec{\rho} = \mathcal{S}_{\mathrm{SWAP}} \boldsymbol{\mathcal{X}} \cdot \vec{\boldsymbol{\Delta}}_\rho, \tag{6.17}$$

where $\otimes$ represents the Kronecker product between matrices, $\vec{\boldsymbol{\Delta}}_\rho$ is a D^2-dimensional vector containing the diagonals of ρ—given by $|\vec{\boldsymbol{\rho}}_k\rangle$—stacked on top of each other, $\mathcal{S}_{\mathrm{SWAP}}$ is a $D^2 \times D^2$-matrix that acts as $\mathcal{S}_{\mathrm{SWAP}}(|j\rangle \otimes |k\rangle) = |k\rangle \otimes |j\rangle$, and

$$\boldsymbol{\mathcal{X}} = \left(\sum_{m=0}^{D-1} \mathcal{X}^m \otimes |m\rangle\langle m| \right). \tag{6.18}$$

Finally, after taking Eqs. (6.10), (6.12), (6.14), (6.15), and (6.17) into account, the components of ρ can be isolated by computing

$$\mathcal{G} = \sum_{m=0}^{D-1} |m\rangle\langle m| \otimes \mathscr{G}_m, \tag{6.19}$$

$$\mathcal{G}^{\dashv} = \sum_{m=0}^{D-1} |m\rangle\langle m| \otimes \mathscr{G}_m^{\dashv}, \tag{6.20}$$

and

$$\begin{aligned} \vec{\rho} &= \mathcal{S}_{\mathrm{SWAP}} \, \boldsymbol{\mathcal{X}} \, \mathcal{G}^{\dashv} \, \mathrm{vec}(\widetilde{\mathcal{P}}) \\ &= \left(\mathcal{S}_{\mathrm{SWAP}} \, \boldsymbol{\mathcal{X}} \, \mathcal{G}^{\dashv} \right) \left((\mathcal{F} \otimes \mathbb{I}_{s_{\max}}) \, \mathrm{vec}(\mathcal{P}) \right), \end{aligned} \tag{6.21}$$

where $x^{\dashv}$ denotes the Moore-Penrose pseudoinverse [134] matrix of x, $\mathbb{I}_{s_{\max}}$ is a $s_{\max} \times s_{\max}$ identity matrix, and $\mathrm{vec}(\mathcal{P})$ is the vectorization of matrix $\mathcal{P}$ (see Appendix of [110]). We have used Eq.A.3 of of [110] in order to write $\mathrm{vec}(\mathcal{P}\mathcal{F}) = (\mathcal{F} \otimes \mathbb{I})\,\mathrm{vec}(\mathcal{P})$, being $\mathcal{F}$ a symmetric matrix. We have resorted to vectorized versions of some matrices as these allow one to write efficient numerical codes. The use of sparse matrices, as explained in Sec. 6.2, may contribute substantially to the efficiency of the computation of $\vec{\rho}$ for quantum systems of very high dimensions. Matrix pseudoinverse has been used instead of the usual matrix inverse because $\mathcal{G}$ contains $Ds_{\max}$ rows and D^2 columns and, consequently, may be not square. Equation (6.21), in summary, relates the components of the reconstructed density matrix—stored in vector $\vec{\rho}$—with the experimental measurements ($\mathcal{P}$) and the measurement settings ($\mathcal{G}$) in an explicit way. The density operator ρ is obtained by just rearranging the elements of $\vec{\rho}$ in a square matrix, which can be post-processed if required. Large parentheses in Eq. (6.21) indicate the recommended multiplication order with the goal of optimizing the use of memory.

Comparison with general linear inversion

Let us consider an arbitrary M-outcome quantum measurement described by POVM elements Π_μ, where $\mu = 1, \ldots, M$. If $\vec{p}$ is a vector containing the probabilities associated with this measurement, it can be shown [see Eq.A.5 of of [110]] that $\vec{p} = \mathcal{M}\vec{\rho}$, where

$$\mathcal{M} = \left(\sum_{\mu=1}^{M} |\mathrm{vec}(\Pi_\mu)\rangle\langle\mu| \right)^{\dagger}. \tag{6.22}$$

Thus, a simple way to obtain $\vec{\rho}$ is by means of $\vec{\rho} = \mathcal{M}^{\dashv}\vec{p}$. If the set of measurements is not informationally complete, there will be ambiguities in the state, i.e., there can exist several solutions $\vec{\rho}$ for the problem $\vec{p} = \mathcal{M}\vec{\rho}$ and, thus, we should expect the performance of the reconstruction to be poor in terms of fidelity, as it may depend highly on the algorithm used to compute $\mathcal{M}^{\dashv}$. The use of informationally complete measurements eliminates these ambiguities.

Moreover, the computation of $\mathcal{M}^{\dashv}$ for the method studied in this article might be infeasible in very high dimensions as it requires (i) being able to store in memory a highly dense matrix $\mathcal{M}$ of size $D^2 \times Ds_{\max}$, and (ii) the ability of computing its pseudoinverse. For instance, matrix $\mathcal{M}$ for a 8-qubit system ($D = 256$, $s_{\mathrm{max}} = 384$) requires 96 GB of memory for the sole purpose of being stored using complex double-precision floating-point numbers. Thus, the computation of $\mathcal{M}^{\dashv}$ for a multiqubit/multiqudit system might be impractical in most current computers.

On the other hand, we may see from the previous section that matrices $\mathcal{S}_{\mathrm{SWAP}}$, $\mathfrak{X}$, $\mathcal{G}^{\dashv}$, and $(\mathcal{F} \otimes \mathbb{I}_{s_{\mathrm{max}}})$ are very sparse for high dimensions: their densities (ratio of nonzero elements) are $1/D^2$, $1/D^2$, $1/D$, and $1/s_{\mathrm{max}}$, respectively. Consequently, the aforementioned matrices for the 8-qubit case require less than 1 GB of memory each when using sparse matrices[2], making now the computations possible in many computers.

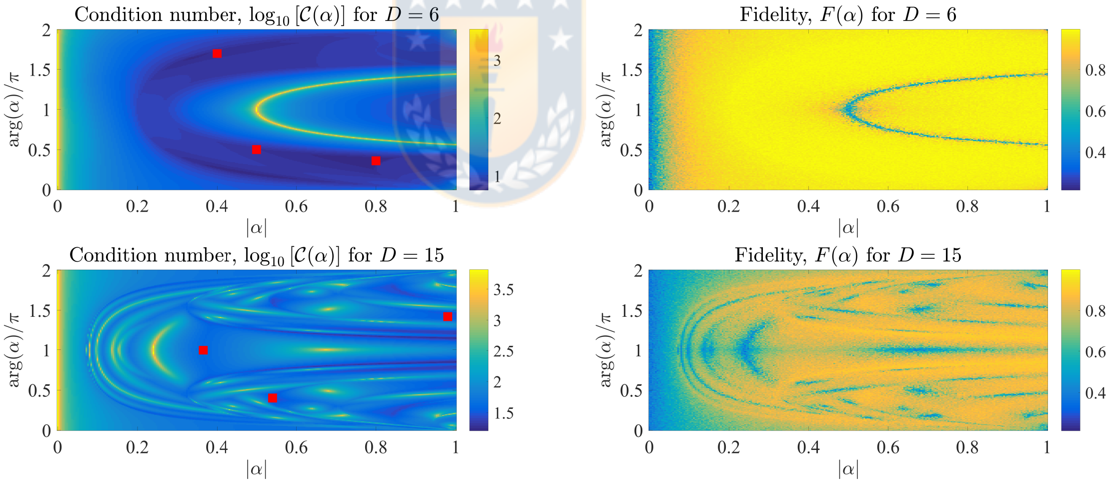

Figure 6.1: Left panels: Condition number $\mathcal{C}\left(\mathcal{G}(\alpha)\right)$ as function of α—given that fiducial state $|\alpha_0\rangle$ is given by Eqs. (6.24) and (6.25)—for dimensions 6 and 15. Red squares indicate the values of α that were used in the experiment reported in this article. Since $\mathcal{C}\left(\mathcal{G}(\alpha)\right)$ might adopt very different values, these graphs were presented in logarithmic scale. Right panels: Fidelity of reconstructed states simulated by Monte Carlo method.

---

[2] Numerical tests for the 8-qubit case show that $(\mathcal{F} \otimes \mathbb{I}_{s_{\mathrm{max}}})$ and $\mathcal{G}^{\dashv}$ require 576.75 MB each, whereas $\mathcal{S}_{\mathrm{SWAP}}$ and $\mathfrak{X}$ need only 1.5 MB each.

Due to finite statistic effects and experimental error sources, the estimates generated via linear inversion might not be positive semidefinite matrices, and thus cannot be accepted as physical states. To solve this problem, several statistical inference techniques can be employed. In particular, maximum likelihood estimation (MLE). This is formulated as an optimization process on the space of the physical states whose output is the state with the highest probability of generating the experimentally acquired data. MLE requires an initial guess. This is chosen in our case as the matrix provided by linear inversion, which contributes to speed up the convergence of MLE. Thus, both MLE and linear inversion are employed to generate physically acceptable estimate. MLE is formulated as an optimization problem on an exponentially scaling number of variables, and thus its computational feasibility is constrainted by the available computing power. Recently, efficient techniques for solving MLE in higher dimensional systems have been proposed [147]. Thereby, the slow convergence of MLE is postponed to even higher dimensions, but not eliminated. In this scenario, linear inversion becomes a viable alternative since it is less computationally demanding than MLE. Moreover, unlike estimates obtained with the help of MLE, the linear inversion process does not exhibit bias [145, 148].

Other alternative approaches such as Forced Purity, Quick and Dirty [88], or searching for the closest density operator [151] are suitable to find physically aceptable states without resorting to numerically demanding optimization problems . All of them require an initial matrix to work on, which can be obtained from $\vec{\rho}$ by linear inversion.

Stability of the inversion

The stability of the inversion under variations of the experimentally obtainable probabilities can be studied by inspecting Eq. (6.21). The problem is either well or ill-conditioned depending on the condition number $\mathcal{C}$ of the matrix involved in the inversion. This, in turn, depends on the singular values of such matrix [40]. As matrices $\mathcal{S}_{\text{SWAP}}$, $\mathfrak{X}$, and $\mathcal{F}\otimes\mathbb{I}_{s_{\max}}$ are all unitary, they do not modify singular values and, hence, matrix $\mathcal{G}$ suffices to analyze the robustness of the tomographic procedure under experimental noise. Indeed,

$$\mathcal{C}\left(\mathcal{S}_{\text{SWAP}}\,\mathfrak{X}\,\mathcal{G}^{-1}\left(\mathcal{F}\otimes\mathbb{I}_{s_{\max}}\right)\right)=\mathcal{C}\left(\mathcal{G}\right)=\frac{\sigma_{\max}\left(\mathcal{G}\right)}{\sigma_{\min}\left(\mathcal{G}\right)},\tag{6.23}$$

where $\sigma_{\max}(\mathcal{G})$ and $\sigma_{\min}(\mathcal{G})$ stand for the maximal and minimal singular values of $\mathcal{G}$, respectively. It can be concluded from Eqs. (6.12), (6.19), and (6.23) that a study of $\mathcal{C}(\mathcal{G})$ as function of $|\alpha_0\rangle$ allows one to predict whether a given fiducial state will be a good choice for quantum tomography. A small condition number indicates that the fiducial state is a good candidate for building the tomographic method.

As $\mathcal{C}(\mathcal{G})$ depends on D complex parameters, its optimization over the Hilbert space does not seem to be computationally easy. For sake of simplicity, we will resort to the notation used in Ref. [125] in order to analyze $\mathcal{C}(\mathcal{G})$ in terms of a single complex parameter α. Thus, the fiducial state will be given by

$$|\alpha_0(\alpha)\rangle = \sum_{k=0}^{D-1} \sqrt{\frac{\lambda_k(\alpha)}{D}}|k\rangle, \tag{6.24}$$

where

$$\lambda_k(\alpha) = 1 - |\alpha| \frac{\sin\left(\frac{k\pi + (D-1)\arg(\alpha)}{D}\right)}{\sin\left(\frac{k\pi - \arg(\alpha)}{D}\right)}. \tag{6.25}$$

Left panels of Figure 6.1 show the decimal logarithm of $\mathcal{C}(\mathcal{G})$ as a function of the absolute value and phase of α for dimensions 6 and 15. As it can be observed, $\mathcal{C}(\mathcal{G}(\alpha))$ can adopt values ranging from $\sim 10^1$ to $\sim 10^5$. Right panels show the fidelity of the reconstruction via Monte Carlo simulations, in which the simulated number of counts by measurement had Poisson noise added. As many simulations were performed, we implemented the "Quick and Dirty" method [88] for post-processing the density operator in Figure 6.1. Direct comparison of left and right panels indicate that numerical instability (high condition number) may introduce a significant inaccuracy in the estimate of the density matrix. This further motivated us to look for adequate fiducial states before making measurements.

In each of the left panels of Figure 6.1, three red squares highlight the values of α that were used for our experiment. These values, also displayed in Table 6.2, were chosen from regions at the figures exhibiting small condition numbers. We have dealt with the problem of numerical stability by choosing fiducial states such that $\mathcal{C}(\mathcal{G})$ adopts small values. Instead of resorting to a given parametrization, we could have generated a large set of random fiducial states and compute the value of $\mathcal{C}(\mathcal{G})$ for each one. If done so, condition numbers even lower than the

D	α_1	α_2	α_3
6	$0.4\, e^{1.7\pi i}$	$0.8\, e^{0.36\pi i}$	$0.5\, e^{0.5\pi i}$
	(7.796)	(6.848)	(8.946)
15	$0.365\, e^{\pi i}$	$0.54\, e^{0.4\pi i}$	$0.98\, e^{1.42\pi i}$
	(40.94)	(27.32)	(33.15)

Table 6.2: Values of α chosen for experimental purposes. Numbers in parentheses below each α indicate the condition number, which is extracted from data of Figure 6.1.

ones used here could be obtained. Nonetheless, using the former procedure we were able to ensure the states on a neighborhood with small condition numbers to have a more robust reconstruction in the case of having noise due to experimental imperfections.

6.3 Experiment

Our setup is depicted in Fig. 6.2. It consists of two main blocks: the *state preparation* (SP) and *projective tomographic measurement* (PM) stages. In SP, weak coherent states are produced resorting to a 690 nm continuous-wave single-mode laser heavily attenuated with calibrated optical filters (not shown in Fig. 6.2 for sake of simplicity) and modulated with an Acousto-Optic Modulator (AOM) configured at a repetition rate of 30 Hz. The mean photon number per pulse is set to $\mu = 0.9$. Consequently, this source works as an approximation to a nondeterministic single-photon source since pulses with a single photon account for 62.3% of the generated non-null pulses [69]. Contributions of multiphoton events to the recorded statistics is strongly suppressed by using a detection window much smaller than the optical pulse duration. Lastly, extra polarizing cubes with an overall extinction ratio greater than 10^{-7} are used to ensure a high quality of horizontal polarization of the transmitted photons. In this way, we are able to attain a high purity degree for the high-dimensional states generated with the spatial light modulators [168].

SLMs are a central part of our setup. Each pixel of a SLM is part of a twisted nematic liquid crystal display (LCD) whose birefringence can be controlled by means of standard video signals emitted by a field programable gate array (FPGA).

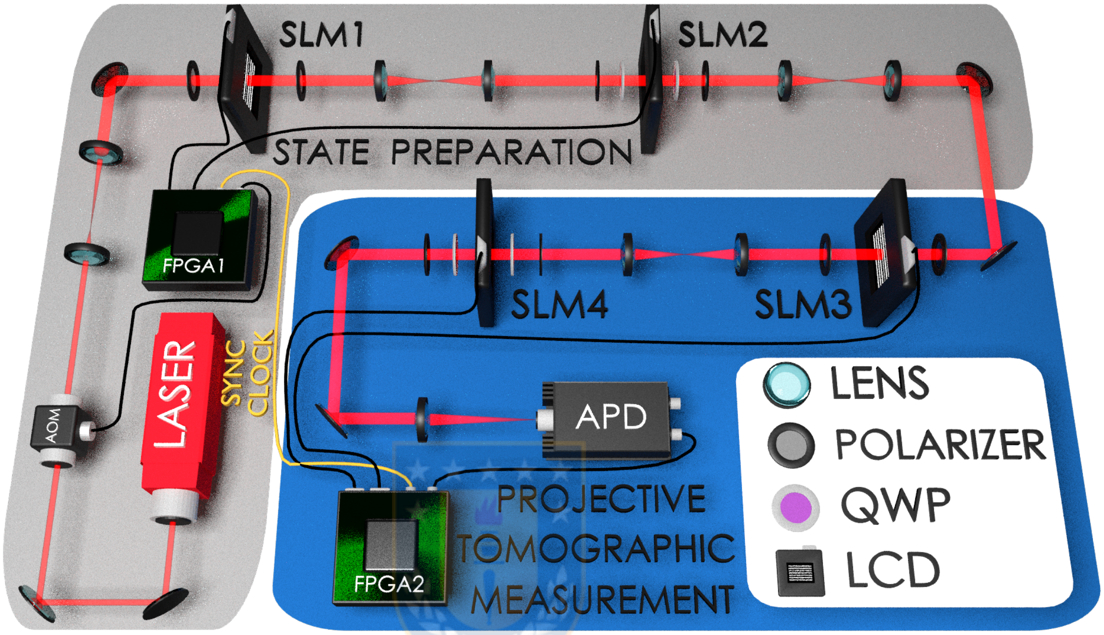

Figure 6.2: Experimental setup.

As a result of an adecquate control of the photon polarization before and after crossing the LCD, we can set the SLM to work as an amplitude-only spatial light modulator (SLM1 and SLM3) or a as a phase-only modulator (SLM2 and SLM4) [116]. Arrays of D slits are displayed on SLM1, each having a width of 96 μm and transmittance coefficients t_ℓ. The centers of contiguous slits are separated by 192 μm. An imaging system projects the image of SLM1 on SLM2, where phases ϕ_ℓ are added to each slit. Thus, the state of the single photons transmitted by these SLMs is $|\Psi\rangle \propto \sum_{\ell=0}^{D-1} \sqrt{t_\ell} e^{i\phi_\ell} |\ell\rangle$—where $|\ell\rangle$ denotes the state of the photon transmitted by the ℓth-slit of the SLMs—and it represents a D-dimensional quantum system encoded into the linear transverse momentum of the photons [120, 101, 100].

To test our new tomographic method we considered 3 different types of states for dimension $D = 6$ and $D = 15$. The reason for choosing such dimensions are: (i) to illustrate the relevance of our method while considering even and odd dimensions, and (ii) the tomographic method based on mutually unbiased bases can not be used in these dimensions. To be more specific, the prepared states were

$$\left|\Psi_1^6\right\rangle = \frac{1}{\sqrt{6}}\sum_{j=0}^{5}|j\rangle, \tag{6.26a}$$

$$\left|\Psi_2^6\right\rangle = |0\rangle, \tag{6.26b}$$

$$\begin{aligned}\left|\Psi_3^6\right\rangle = \frac{1}{\sqrt{6}}\Big[\Big(|0\rangle + |2\rangle\Big) + e^{-i\pi/4}|4\rangle \\ + e^{-i\pi/8}\Big(|1\rangle + |3\rangle + |5\rangle\Big)\Big],\end{aligned} \tag{6.26c}$$

for dimension 6, and

$$\left|\Psi_1^{15}\right\rangle = \frac{1}{\sqrt{15}}\sum_{j=0}^{14}|j\rangle, \tag{6.27a}$$

$$\left|\Psi_2^{15}\right\rangle = |7\rangle, \tag{6.27b}$$

$$\begin{aligned}\left|\Psi_3^{15}\right\rangle = \frac{1}{\sqrt{15}}\Big[&\Big(|0\rangle + |5\rangle + |8\rangle + |14\rangle\Big) \\ &+ e^{-i\pi/10}\Big(|1\rangle + |3\rangle + |9\rangle + |12\rangle\Big) \\ &+ e^{-i\pi/9}|2\rangle + e^{-i\pi/8}\Big(|6\rangle + |11\rangle\Big) \\ &+ e^{-i\pi/7}\Big(|4\rangle + |10\rangle\Big) \\ &+ e^{-i\pi/6}\Big(|7\rangle + |13\rangle\Big)\Big].\end{aligned} \tag{6.27c}$$

for dimension 15.

The Projective Tomographic Measurement stage contains SLM3 and SLM4, used for post-selecting the state to be detected. For this purpose, a new set of transmittance coefficients τ_ℓ and phases ζ_ℓ are used on SLM3 and SLM4, respectively. Finally, detection is performed at the center of the focal plane of a lens located after SLM4 using an avalanche single-photon detector (APD) with a 10 μm-wide pinhole placed in front of it. The probability of detecting a single photon is, thus, proportional to $|\langle\Theta|\Psi\rangle|^2$ [100, 57, 157], where $|\Theta\rangle \propto \sum_\ell \sqrt{\tau_\ell}e^{-i\zeta_\ell}|\ell\rangle$. In our case, $|\Theta\rangle$

represents each of the states $|\alpha_{sj}\rangle$ on which the measurements are performed, so parameters τ_ℓ and ζ_ℓ are adjusted accordingly. In order to show the possibility of using different fiducial states, we used $|\alpha_0(\alpha_k)\rangle$ [see Eq. (6.24)] as the fiducial state for reconstructing state $|\Psi_k^D\rangle$, where the values of α_k are the ones shown in Table 6.2.

Each projective measurement related to our tomographic method was repeated 10 times, which allowed us to obtain its associated mean value of detection counts. We denote $n_{sj,r}$ as the counts obtained from measuring Π_{sj} in the rth round of measurements, where $r = 1, \ldots, 10$. Average numbers of counts $\bar{n}_{sj}$ can then be obtained by

$$\bar{n}_{sj} = \frac{1}{10} \sum_{r=1}^{10} n_{sj,r}. \tag{6.28}$$

Measurements were taken for times long enough to obtain around $10000 \times D$ counted photons, as a total over all projections Π_{sj}, for each round. Once all the detection counts were recorded and the average probabilities were computed, we proceeded to the post-measurement processing of the data. Error margins for density matrices and its corresponding figures of merit were determined through 10000 Monte Carlo simulations for each reconstructed state. Simulated counts numbers $n_{sj}^{(\mu)}$ are obtained by adding Poisson noise to the originally averaged data, where μ denotes the number of the Monte Carlo trial and ranges from 1 to 10000. Only in the first case there is no noise considered, i.e.,

$$n_{sj}^{(\mu)} = \begin{cases} \bar{n}_{sj}, & \text{for } \mu = 1, \\ \text{Poisson}\left(\bar{n}_{sj}\right), & \text{otherwise.} \end{cases} \tag{6.29}$$

Afterwards, simulated probability matrices $\mathcal{P}^{(\mu)}$ are computed for each Monte Carlo trial according to

$$\mathcal{P}^{(\mu)} = \frac{\displaystyle\sum_{s=0}^{s_{\max}-1} \sum_{j=0}^{D-1} n_{sj}^{(\mu)} |s\rangle\langle j|}{\displaystyle\sum_{t=0}^{s_{\max}-1} \sum_{k=0}^{D-1} n_{tk}^{(\mu)}}, \tag{6.30}$$

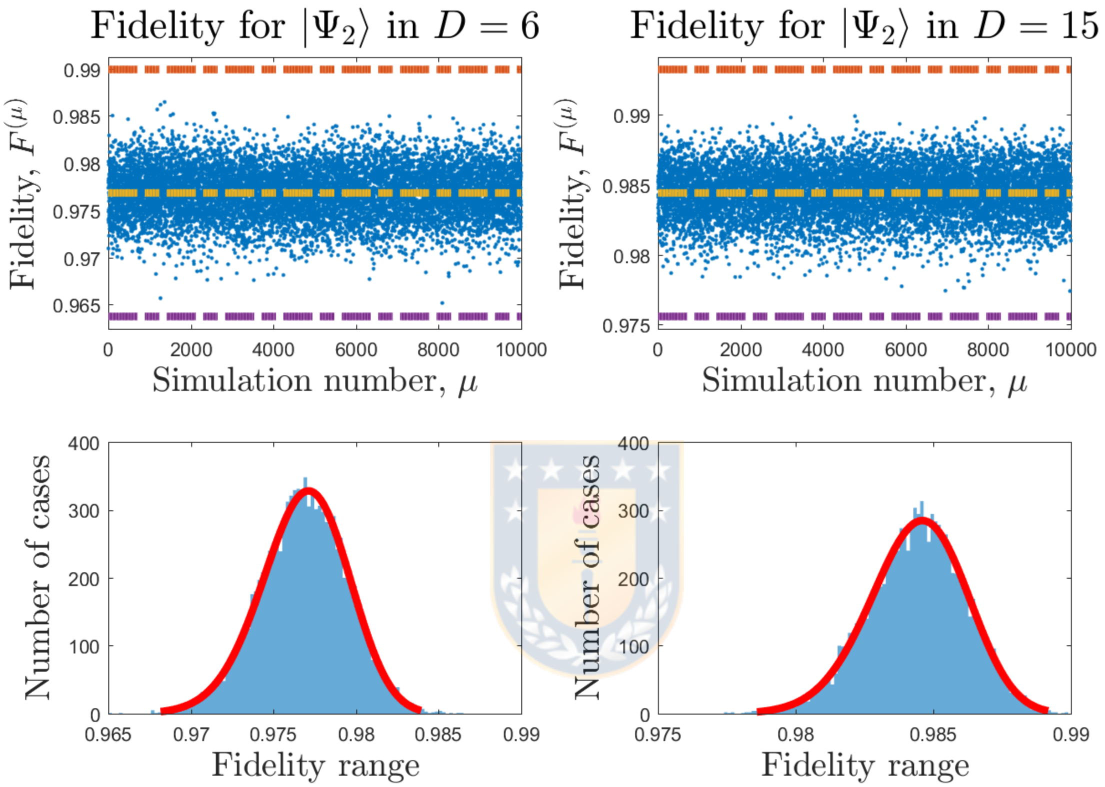

Figure 6.3: Examples of the Monte Carlo simulations performed (uppper panels) and their respective histograms (lower panels). Three horizontal dot-dashed lines in the upper graphs represent the mean value ($\langle F \rangle$) of the simulations and the $\langle F \rangle \pm 5\sigma$ interval. The continuous line in each histogram represents a fitted beta distribution. For each fitted function, the probability of having a value outside the $\pm 5\sigma$ interval is $\sim 10^{-6}$.

where Eq. (6.8) was taken into account. Then, matrix $\mathcal{P}^{(\mu)}$ is used in Eq. (6.21) in order to obtain a reconstructed density matrix $\rho^{(\mu)}$. As Eq. (6.21) cannot ensure its positiveness, maximum likelihood estimation (MLE) was subsequently employed (see Appendix of [110] for details) in order to ensure matrix positiveness [81, 85, 165]. The fidelity $F^{(\mu)}$ between $\rho^{(\mu)}$ and the state $|\Psi\rangle$ we intended to prepare is computed as figure of merit for each state resulting from MLE, where

$$F^{(\mu)} = \langle\Psi|\rho^{(\mu)}|\Psi\rangle. \tag{6.31}$$

The final result for the fidelity is expressed in terms of the mean and standard deviation of the simulated results, that is,

$$F = \left\langle \left\{ F^{(\mu)} \right\} \right\rangle \pm 5\sigma\left(\left\{ F^{(\mu)} \right\} \right). \tag{6.32}$$

Two examples of the Monte Carlo simulations are shown in Fig. 6.3. We have chosen ±5σ as error margins since the probability of obtaining a value outside it in a new round of experiments is less than 10^{-6} in the case the values of $F^{(\mu)}$ distribute around their mean value following a normal distribution. In the worst-case scenario, such probability is less than 4%, according to the Bienaymé-Chebyshev inequality. The reconstructed density operators in dimension 6 are depicted in Fig. 6.4, whereas Fig. 6.5 illustrate the results for dimension 15. A summary of the results is shown in Table 6.3. As it can be seen, high values of fidelities were obtained. More specifically, for dimension 6 (15) an overall fidelity of 0.977 (0.957) has been recorded, while considering an ensemble of only 6×10^4 (1.5×10^5) events of photo-detection for the state reconstruction procedure. In the literature there are several experiments toward quantum tomography of a single qudit: Ref. [100] reported the experimental realization of tomography using mutually unbiased bases and they obtained fidelities of 0.96 ± 0.03 and 0.93 ± 0.03 for dimensions 7 and 8, respectively. Ref. [71] reported 0.985 ± 0.015 for $D = 8$ using a method designed for reconstructing pure states. The experiment of Ref. [18] using SIC-POVM obtained fidelities of 0.960 ± 0.003 and 0.887 ± 0.003 for dimensions 6 and 10, respectively. Our experimental results compare favorably with these previous results, which validates the good performance of the experimental setup employed to realize the quantum tomography assisted by multiply symmetric states in higher dimensions.

6.4 Concluding remarks

In summary, we have reported the experimental realization of quantum state tomography assisted by multiply symmetric states for dimensions $D = 6$ and

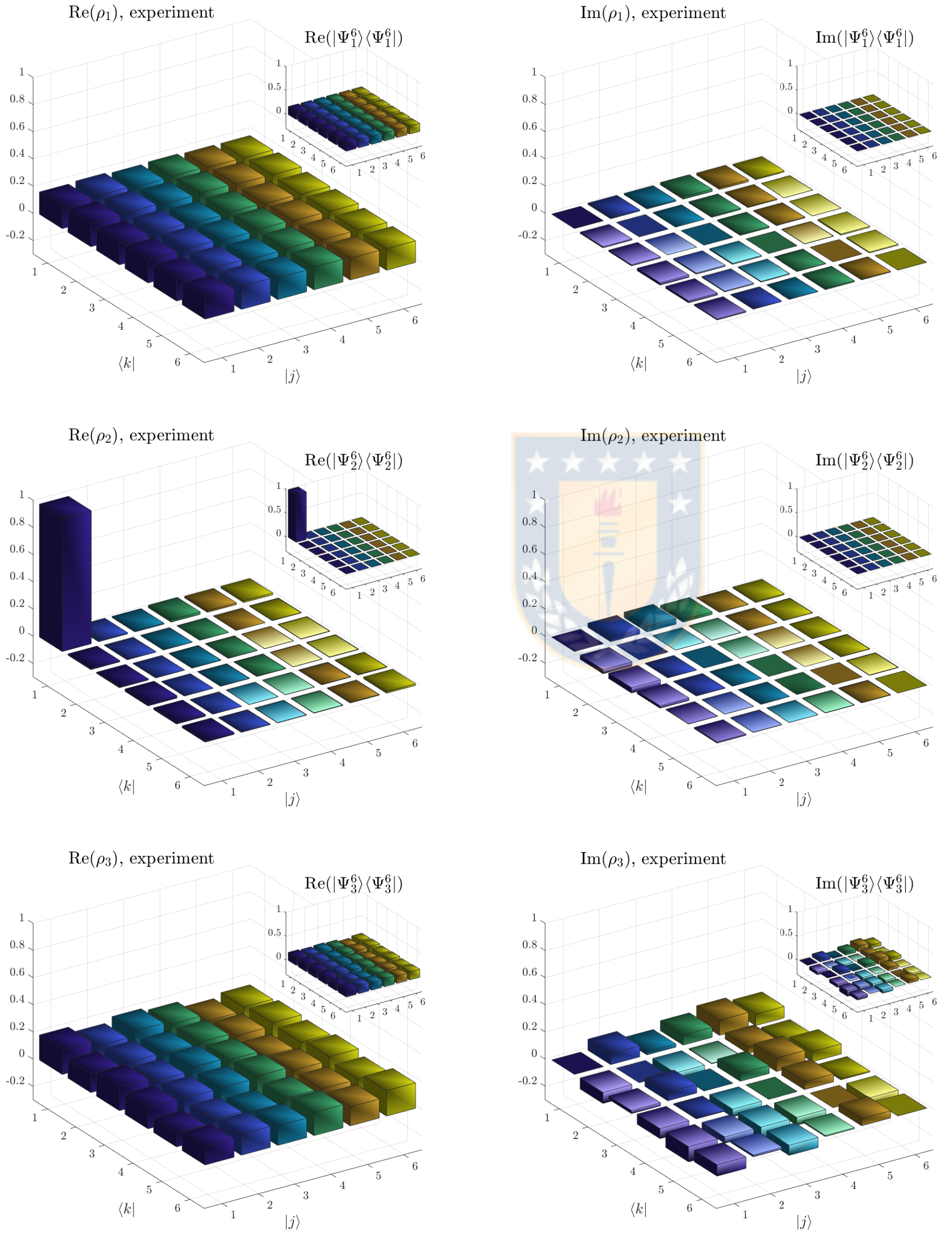

Figure 6.4: Reconstructed quantum states for D = 6. The insets show the theoretically expected results.

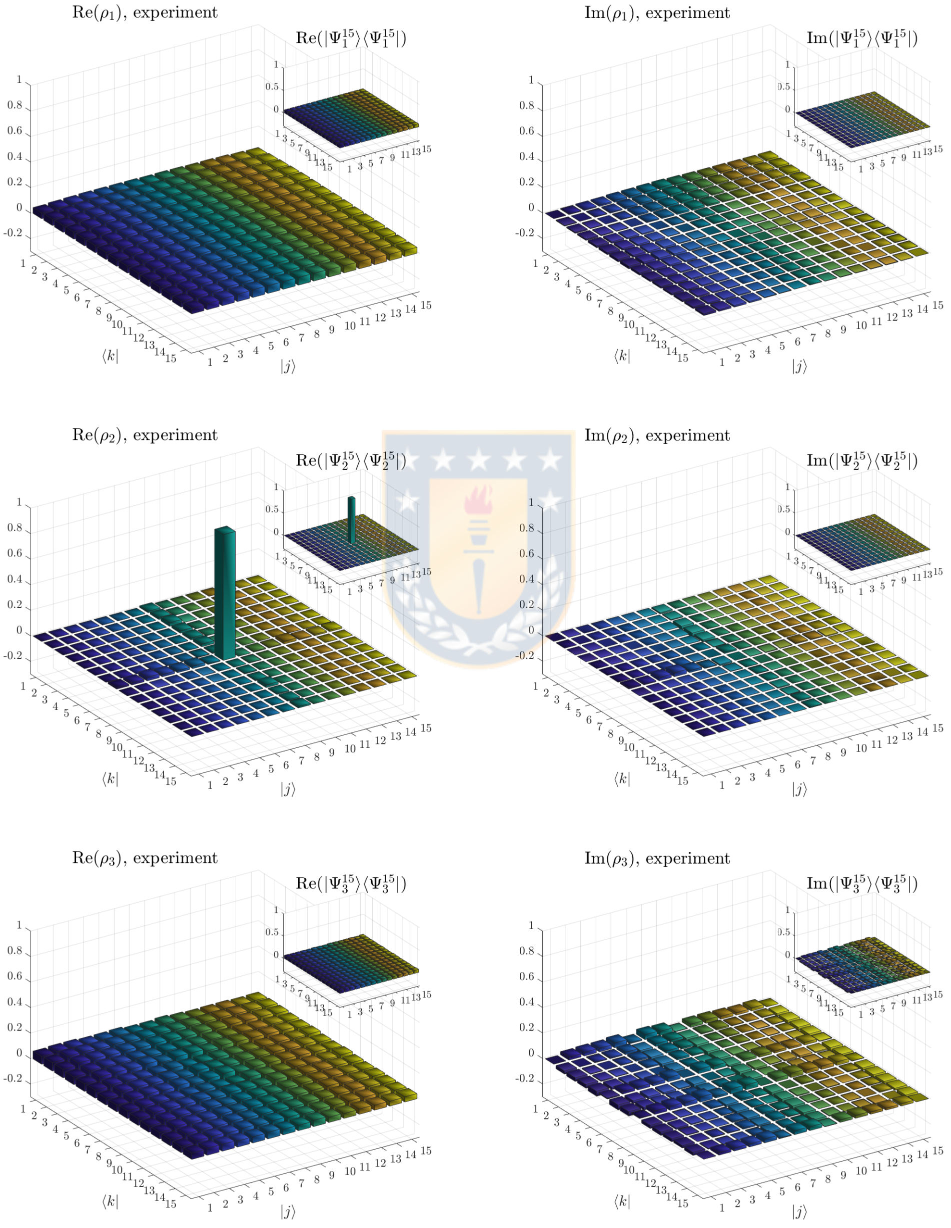

Re(ρ_1), experiment

Re($|\Psi_1^{15}\rangle\langle\Psi_1^{15}|$)

Im(ρ_1), experiment

Im($|\Psi_1^{15}\rangle\langle\Psi_1^{15}|$)

Re(ρ_2), experiment

Re($|\Psi_2^{15}\rangle\langle\Psi_2^{15}|$)

Im(ρ_2), experiment

Im($|\Psi_2^{15}\rangle\langle\Psi_2^{15}|$)

Re(ρ_3), experiment

Re($|\Psi_3^{15}\rangle\langle\Psi_3^{15}|$)

Im(ρ_3), experiment

Im($|\Psi_3^{15}\rangle\langle\Psi_3^{15}|$)

Figure 6.5: Reconstructed quantum states for D = 15. The insets show the theoretically expected results.

D	$\lvert\Psi_1^D\rangle$	$\lvert\Psi_2^D\rangle$	$\lvert\Psi_3^D\rangle$
6	0.998 ± 0.001	0.977 ± 0.013	0.956 ± 0.010
15	0.965 ± 0.006	0.984 ± 0.009	0.922 ± 0.007

Table 6.3: Fidelities obtained for each of the reconstructed states, with their respective 5σ uncertainty extracted from 10000 Monte Carlo trials. MLE was used in each trial.

$D = 15$. Unlike MUB and SIC-POVM tomographic methods, this method is guaranteed to exist in any dimension and provides a significant reduction in the number of measurement outcomes when compared to standard quantum tomography. Furthermore, in the case of odd dimensions the method requires the least possible number of measurement outcomes. As explained in Sec. 6.2, this tomographic method is different from a general linear inversion in the sense that (i) multiply symmetric states constitute an informationally complete set of measurements, and (ii) it was possible to rewrite the equations in such a way the inversion is represented now in terms of multiplying sparse matrices and computing inverses of smaller matrices rather than computing the inverse of a large matrix, which is more practical for high dimensions. The POVM elements used for this reconstruction method, as Eq. (6.6) shows, depend on a given fiducial state $|\alpha_0\rangle$ that can be freely chosen. Nevertheless, this fiducial state is chosen in such a way the inversion algorithm remains numerically stable. Such stability can be analyzed in terms of the condition number of matrix $\mathcal{G}$ of Eq. (6.19).

Further improvements can be obtained by studying the condition number. We have reduced the complexity of this problem by studying fiducial states defined by two parameters, which led to condition numbers of the order of 10. However, Monte Carlo simulations with randomly generated fiducial states have shown that smaller condition numbers are possible. Other continuation of the current work concerns the case of multipartite systems. For instance, the state of a two-qudit system can be estimated with a minimal number of D^4 measurement outcomes. This can be achieved for D odd by conditional local estimations employing quantum tomography assisted by multiply symmetric states.

Recently, QT has been studied from the point of view of the achievable estimation accuracy. Here, the figure of merit is the Gill-Massar lower bound $\bar{I} = (D^2 - 1)(D + 1)/4N$ for the infidelity, where N is the size of the ensemble of identically, independently prepared copies of the unknown state to be estimated. This is the highest estimation accuracy for mixed states that can be achieved by means of local measurements, that is, measurements that are carried out on individual members of the ensemble. It has been demonstrated that two-stage quantum tomography for a single qudit approaches $\bar{I}$ [136]. In the first stage of this adaptive tomographic method a small ensemble is employed to obtain a first estimate via standard quantum tomography. This estimate's eigenstates are employed to represent the D^2-1 generators of SU(D), which are subsequently measured in a second stage of standard quantum tomography. For $D=2$ two-stage quantum tomography saturates the Gill-Massar lower bound [106, 80]. However, for $D>2$ this is not the case. Furthermore, numerical evidence suggests that the estimation accuracy behaves as $\bar{I}D$. It is possible to improve the accuracy by modifying two-stage quantum tomography. Instead of projecting onto the eigenstates of the D^2-1 Gell-Mann generators, it is possible to gather enough information to estimate an unknown state by projecting onto $2D+1$ $(2D-1)$ bases for D odd (even). The adaptive version of this method leads to an estimation accuracy that behaves as $2\bar{I}$ [135], independently of the dimension. Here arises the question whether an adaptive version of quantum tomography assisted by multiply symmetric states would lead to an estimation accuracy better than $2\bar{I}$ with the added benefit of a reduced number of total measurement outcomes.

CHAPTER 7

Conclusion

In this dissertation we explored the generation of high dimensional qudits. We accomplished the generation of such states and also we performed projective measurements on them. The experimental setup is completely automated, using the advantages that SLMs and FPGA give. The optical system is robust against misalignment, and because of that, we can perform measurements for large amounts of time (in the order of 30 days). The visibility of the output signal rounds 0.98, allowing the realization of experiments where the violation of tight bounds is not possible with low visibility. Finally I'd like to remark that the versatility of the experimental setup its mainly due to the reconfigurability of the SLMs. We performed three experiments using the presented techniques, that count as follows:

- Certifying an Irreducible 1024-Dimensional Photonic State Using Refined Dimension Witnesses. *Phys. Rev. Lett.*, 120(23):230503 [3].
- High-Dimensional Quantum Communication Complexity beyond Strategies Based on Bells Theorem. *Phys. Rev. Lett.*, 121(15):150504 [111].
- Experimental quantum tomography assisted by multiply symmetric states in higher dimensions. *Phys. Rev. A*, 99(012336) [110].

Said that, I can conclude that the TLM of single photons is an excellent candidate to codify qudits to be used un QI and QC protocols.

Nevertheless, there are a few backwards in our system. Due to the video protocols that control the SLMs, its native repetition rate is 60 Hz. Furthermore, we work using weak coherent pulses in the single photon level. This two considerations leads to low detection statistics. A second backward relies on the dicotomic outcomes of the APD (0 or 1 count) and the fact that we can only project one $\langle\phi|$ per pulse, taking as result that our system have a unique outcome per pulse.

Even when we count the backwards of the experimental scheme, because its versatility, this setup is going to be productive for the next years in the field of QI. If one think objectively, most of the experiments in QI try to measure $|\langle\phi|\psi\rangle|^2$, just as this setup is intended to.

CHAPTER 8

Conclusión

Durante esta disertación exploramos la generación de estados cuánticos en altas dimensiones. Logramos generar dichos estados y realizar mediciones proyectivas sobre ellos. El esquema experimental está completamente automatizado, siendo parte fundamental del sistema de control la electrónica programable basada en FPGAs. El sistema óptico es robusto ante desalineación, por ende es posible realizar experimentos continuos por largos tiempos (en el orden de 30 días). La visibilidad de la seal de salida ronda el 98%, permitiendo realizar experimentos que necesitan altas fidelidades, por ejemplo cuando es necesario superar límites de funciones de interés. Finalmente remarcamos que versatilidad que tiene este arreglo experimental se debe en buena medida a las reconfigurabilidad de los SLMs, siendo parte esencial en nuestro sistema.

Con dicho setup, realizamos tres experimentos en donde una visibilidad alta era un requerimiento crucial para lograrlo.

- Certifying an Irreducible 1024-Dimensional Photonic State Using Refined Dimension Witnesses. *Phys. Rev. Lett.*, 120(23):230503 [3].
- High-Dimensional Quantum Communication Complexity beyond Strategies Based on Bells Theorem. *Phys. Rev. Lett.*, 121(15):150504 [111].
- Experimental quantum tomography assisted by multiply symmetric states in higher dimensions. *Phys. Rev. A*, 99(012336) [110].

Dicho esto podemos concluir que el TLM de fotones individuales es un excelente candidato para codificar qudits y realizar protocolos de QI y QC.

Sin embargo, existen algunas desventajas en nuestro sistema. Debido a que las señales que controlan los SLMs se rigen por protocolos de video convencionales, su tasa de repetición es de 60 Hz. Aunado a esto, nosotros trabajamos en el régimen de fotones individuales. Estas dos consideraciones tienen como resultado que la estadística de adquisición del sistema sea muy baja y que no puede ser superada debido a la electrónica nativa de los SLM. Una segunda desventaja es que debido a la naturaleza dicotómica de las mediciones (esto quiere decir que al hacer la proyección $|\langle\phi|\psi\rangle|$ los únicos valores posibles en el detector son 0 o 1 en cada pulso) y a que solo puedo proyectar un solo $\langle\phi|$ por pulso, nuestro sistema ve una única *outcome* a la vez.

Aún contando las desventajas del esquema experimental, este arreglo va a seguir produciendo buenos resultados para los avances en el campo de la QI debido a su versatilidad. Si uno piensa de manera concreta, el objetivo de la mayor parte de los experimentos cuánticos es medir $|\langle\phi|\psi\rangle|^2$ que es el objetivo del sistema aquí presentado.

Bibliography

[1] Agnew, M., Bolduc, E., Resch, K. J., Franke-Arnold, S., and Leach, J. (2014). Discriminating Single-Photon States Unambiguously in High Dimensions. *Phys. Rev. Lett.*, 113(2):020501.

[2] Aguilar, E., Borkała, J., Mironowicz, P., and Pawłowski, M. (2017). Connections Between Mutually Unbiased Bases and Quantum Random Access Codes.

[3] Aguilar, E. A., Farkas, M., Martínez, D., Alvarado, M., Cariñe, J., Xavier, G. B., Barra, J. F., Cañas, G., Pawłowski, M., and Lima, G. (2018). Certifying an Irreducible 1024-Dimensional Photonic State Using Refined Dimension Witnesses. *Phys. Rev. Lett.*, 120(23):230503.

[4] Ahrens, J., Badziag, P., Cabello, A., and Bourennane, M. (2012). Experimental device-independent tests of classical and quantum dimensions. *Nat. Phys.*, 8(8):592–595.

[5] Ali-Khan, I., Broadbent, C. J., and Howell, J. C. (2007). Large-Alphabet Quantum Key Distribution Using Energy-Time Entangled Bipartite States. *Phys. Rev. Lett.*, 98(6):060503.

[6] Ambainis, A., Leung, D., Mancinska, L., and Ozols, M. Quantum Random Access Codes with Shared Randomness.

[7] Ambainis, A., Nayak, A., Ta-Shma, A., and Vazirani, U. (1999a). Dense quantum coding and a lower bound for 1-way quantum automata. In *Proceedings of the 31st Annual ACM Symposium on Theory of Computing (STOC'99)*, pages 376–383.

[8] Ambainis, A., Nayak, A., Ta-Shma, A., and Vazirani, U. (1999b). Dense quantum coding and a lower bound for 1-way quantum automata. In *Proceedings of the Thirty-first Annual ACM Symposium on Theory of Computing*, STOC '99, pages 376–383, New York, NY, USA. ACM.

[9] Appleby, D. M. (2005). Symmetric informationally completepositive operator valued measures and the extended clifford group. *J. Math. Phys.*, 46(052107).

[10] Appleby, D. M., Bengtsson, I., Brierley, S., Ericsson, A., Grassl, M., , and Larsson, J. A. (2014). *Quantum Inf. Comput.*, 14(33960).

[11] Appleby, D. M., Bengtsson, I., Brierley, S., Grassl, M., Gross, D., and Larsson, J. A. (2012). *Quantum Inf. Comput.*, 12(40431).

[12] Appleby, D. M., Chien, T.-Y., Flammia, S., and Waldron, S. (2018). *J. Phys. A: Math. Theor.*, 51(165302).

[13] Arias, M., Cañas, G., Gómez, E. S., Barra, J. F., Xavier, G. B., Lima, G., D'Ambrosio, V., Baccari, F., Sciarrino, F., and Cabello, A. (2015). Testing noncontextuality inequalities that are building blocks of quantum correlations. *Phys. Rev. A*, 92(3):032126.

[14] Bandyopadhyay, S., Boykin, O., Roychowdhury, V., and Vatan, F. (2002). A New Proof for the Existence of Mutually Unbiased Bases. *Algorithmica*, 34(4):512–528.

[15] Barends, R., Kelly, J., Megrant, A., Veitia, A., Sank, D., Jeffrey, E., White, T. C., Mutus, J., Fowler, A. G., Campbell, B., Chen, Y., Chen, Z., Chiaro, B., Dunsworth, A., Neill, C., O'Malley, P., Roushan, P., Vainsencher, A., Wenner, J., Korotkov, A. N., Cleland, A. N., and Martinis, J. M. (2014). Superconducting quantum circuits at the surface code threshold for fault tolerance. *Nature*, 508(7497):500–503.

[16] Barnett, S. M., Gilson, C. R., and Sasaki, M. (2001). Fidelity and the communication of quantum information. *J. Phys. A. Math. Gen.*, 34(35):6755–6766.

[17] Barreiro, J. T., Langford, N. K., Peters, N. A., and Kwiat, P. G. (2005). Generation of hyperentangled photon pairs. *Phys. Rev. Lett.*, 95:260501.

[18] Bent, N., Qassim, H., Tahir, A. A., Sych, D., Leuchs, G., Sánchez-Soto, L. L., Karimi, E., and Boyd, R. W. (2015). Experimental Realization of Quantum Tomography of Photonic Qudits via Symmetric Informationally Complete Positive Operator-Valued Measures. *Phys. Rev. X*, 5(4):041006.

[19] Bernhard, C., Bessire, B., Feurer, T., and Stefanov, A. (2013). Shaping frequency-entangled qudits. *Phys. Rev. A*, 88(3):032322.

[20] Bowles, J., Quintino, M. T., and Brunner, N. (2014). Certifying the dimension of classical and quantum systems in a prepare-and-measure scenario with independent devices. *Phys. Rev. Lett.*, 112:140407.

[21] Brassard, G., Buhrman, H., Linden, N., Méthot, A. A., Tapp, A., and F. Unger, . (2006). Limit on nonlocality in any world in which communication complexity is not trivial,. *Phys. Rev. Lett.*, 96:250401.

[22] Breitenbach, G., Schiller, S., and Mlynek, J. (1997). Measurement of the quantum states of squeezed light. *Nature*, 387(6632):471–475.

[23] Brukner, C., Paterek, T., , and Żukowski, M. (2003). Quantum communication complexity protocols based on higher-dimensional entangled systems. *Int. J. Quantum Inform.*, 01:519.

[24] Brukner, C., Żukowski, M., Pan, J.-W., and Zeilinger, A. (2004). Bell's inequalities and quantum communication complexity. *Phys. Rev. Lett*, 92:127901.

[25] Brukner, Č., Żukowski, M., and Zeilinger, A. (2002). Quantum Communication Complexity Protocol with Two Entangled Qutrits. *Phys. Rev. Lett.*, 89(19):197901.

[26] Brunner, N., Cavalcanti, D., Pironio, S., Scarani, V., and Wehner, S. (2014). Bell nonlocality. *Rev. Mod. Phys*, 86:419.

[27] Brunner, N., Navascués, M., and Vértesi, T. (2013). Dimension witnesses and quantum state discrimination. *Phys. Rev. Lett.*, 110:150501.

[28] Brunner, N., Pironio, S., Acin, A., Gisin, N., Méthot, A. A., and Scarani, V. (2008). Testing the dimension of hilbert spaces. *Phys. Rev. Lett.*, 100:210503.

[29] Bruß, D. and Macchiavello, C. (2002). Optimal Eavesdropping in Cryptography with Three-Dimensional Quantum States. *Phys. Rev. Lett.*, 88(12):127901.

[30] Buhrman, H., Cleve, R., Massar, S., and de Wolf, R. (2010). Nonlocality and communication complexity. *Rev. Mod. Phys*, 82:665.

[31] Buhrman, H., Czekaj, L., Grudka, A., Horodecki, M., Horodecki, P., Markiewicz, M., Speelman, F., and Strelchuk, S. (2016). Quantum communication complexity advantage implies violation of a bell inequality. *PNAS*, 22:113.

[32] Buhrman, H., van Dam, W., Høyer, P., and Tapp, A. (1999). Multiparty quantum communication complexity. *Phys. Rev. A*, 60:2737.

[33] Bužek, V., Derka, R., Adam, G., and Knight, P. (1998). Reconstruction of Quantum States of Spin Systems: From Quantum Bayesian Inference to Quantum Tomography. *Ann. Phys. (N. Y).*, 266(2):454–496.

[34] Cañas, G., Acuña, E., Cariñe, J., Barra, J. F., Gómez, E. S., Xavier, G. B., Lima, G., and Cabello, A. (2016). Experimental demonstration of the connection between quantum contextuality and graph theory. *Phys. Rev. A*, 94(1):012337.

[35] Cañas, G., Arias, M., Etcheverry, S., Gómez, E. S., Cabello, A., Xavier, G. B., and Lima, G. (2014a). Applying the Simplest Kochen-Specker Set for Quantum Information Processing. *Phys. Rev. Lett.*, 113(9):090404.

[36] Cañas, G., Etcheverry, S., Gómez, E. S., Saavedra, C., Xavier, G. B., Lima, G., and Cabello, A. (2014b). Experimental implementation of an eight-dimensional kochen-specker set and observation of its connection with the greenberger-horne-zeilinger theorem. *Phys. Rev. A*, 90:012119.

[37] Cañas, G., Vera, N., ne, J. C., González, P., J.Cardenas, Connolly, P. W. R., Przysiezna, A., Gómez, E. S., Figueroa, M., Vallone, G., Villoresi, P., da Silva, T. F.,

Xavier, G. B., and Lima, G. (2017). High-dimensional decoy-state quantum key distribution over multicore telecommunication fibers. *Phys. Rev. A*, 96:022317.

[38] Casaccino, A., ao, E. F. G., and Severini, S. (2008). Extrema of discrete wigner functions and applications. *Phys. Rev. A*, 78:022310.

[39] Cerf, N. J., Bourennane, M., Karlsson, A., and Gisin, N. (2002). Security of Quantum Key Distribution Using d-Level Systems. *Phys. Rev. Lett.*, 88(12):127902.

[40] Cheney, W. and Kincaid, D. (2008). *Numerical Mathematics and Computing*. Thomson Brooks/Cole, Belmont, CA, 6th edition.

[41] Chuang, I. L. and Nielsen, M. A. (1997). Prescription for experimental determination of the dynamics of a quantum black box. *J. Mod. Opt.*, 44(11-12):2455–2467.

[42] Chuang, I. L., Vandersypen, L. M. K., Zhou, X. L., Leung, D. W., and Lloyd, S. (1998). Experimental realization of a quantum algorithm. *Nature*, 393(6681):143–146.

[43] Cleve, R. and Buhrman, H. (1997). Substituting quantum entanglement for communication. *Phys. Rev. A.*, 56:1201.

[44] Collins, D., Gisin, N., Linden, N., Massar, S., and Popescu, S. (2002). Bell Inequalities for Arbitrarily High-Dimensional Systems. *Phys. Rev. Lett.*, 88(4):040404.

[45] Cong, W., Cai, Y., Bancal, J.-D., and Scarani, V. (2017). Witnessing irreducible dimension. *Phys. Rev. Lett.*, 119:080401.

[46] Cramer, M., Plenio, M. B., Flammia, S. T., Somma, R., Gross, D., Bartlett, S. D., Landon-Cardinal, O., Poulin, D., and Liu, Y.-K. (2010). Efficient quantum state tomography. *Nat. Commun.*, 1(9):149.

[47] Czechlewski, M., Saha, D., and Pawłowski, M. (2018). Efficient device independent dimension witness of arbitrary quantum systems employing binary outcome measurements. *ArXiv e-prints*.

[48] Dada, A. C., Leach, J., Buller, G. S., Padgett, M. J., and Andersson, E. (2011). Experimental high-dimensional two-photon entanglement and violations of generalized Bell inequalities. *Nat. Phys.*, 7(9):677–680.

[49] D'Ambrosio, V., Bisesto, F., Sciarrino, F., Barra, J. F., Lima, G., and Cabello, A. (2014). Device-independent certification of high-dimensional quantum systems. *Phys. Rev. Lett.*, 112:140503.

[50] D'Ariano, G. M., Laurentis, M. D., Paris, M. G. A., Porzio, A., and Solimeno, S. (2002). Quantum tomography as a tool for the characterization of optical devices. *J. Opt. B Quantum Semiclassical Opt.*, 4(3):S127–S132.

[51] D'Ariano, G. M. and Lo Presti, P. (2001). Quantum tomography for measuring experimentally the matrix elements of an arbitrary quantum operation. *Phys. Rev. Lett.*, 86:4195–4198.

[52] D'Ariano, G. M., Maccone, L., and Presti, P. L. (2004). Quantum calibration of measurement instrumentation. *Phys. Rev. Lett.*, 93:250407.

[53] Durt, T., Cerf, N. J., Gisin, N., and Żukowski, M. (2003). Security of quantum key distribution with entangled qutrits. *Phys. Rev. A*, 67(1):012311.

[54] Durt, T., Englert, B.-G., Bengtsson, I., and Życzkowski, K. (2010). On mutually unbiased bases. *Int. J. Quantum Inf.*, 08(04):535–640.

[55] Ekert, A. K. (1992). Quantum cryptography based on bell's theorem. *Phys. Rev. Lett.*, 67.

[56] Epping, M. and Brukner, C. (2013). Bound entanglement helps to reduce communication complexity. *Phys. Rev. A*, 87:032305.

[57] Etcheverry, S., Cañas, G., Gómez, E. S., Nogueira, W. A. T., Saavedra, C., Xavier, G. B., and Lima, G. (2013). Quantum key distribution session with 16-dimensional photonic states. *Sci. Rep.*, 3(1):2316.

[58] Farkas, M. (2018). Self-testing mutually unbiased bases in the prepare-and-measure scenario. *ArXiv e-prints*.

[59] Fickler, R., Campbell, G., Buchler, B., Lam, P. K., and Zeilinger, A. (2016). Quantum entanglement of angular momentum states with quantum numbers up to 10,010. *Proceedings of the National Academy of Sciences*, 113(48):13642–13647.

[60] Fickler, R., Lapkiewicz, R., Plick, W. N., Krenn, M., Schaeff, C., Ramelow, S., and Zeilinger, A. (2012). Quantum entanglement of high angular momenta. *Science*, 338(6107):640–643.

[61] Fitzi, M., Gisin, N., and Maurer, U. (2015). Quantum solution to the byzantine agreement problem. *Phys. Rev. Lett.*, 87.

[62] Flamini, F., Spagnolo, N., and Sciarrino, F. Photonic quantum information processing: a review.

[63] Fuchs, C. A. and Stacey, B. C. (2010). The sic question: History and state of play. *Axioms*, 6(21).

[64] Gallego, R., Brunner, N., Hadley, C., and Acín, A. (2010). Device-independent tests of classical and quantum dimensions. *Phys. Rev. Lett.*, 105:230501.

[65] Galvao, E. F. (2001). Feasible quantum communication complexity protocol. *Phys. Rev. A*, 65:012318.

[66] Gao, W.-B., Lu, C.-Y., Yao, X.-C., Xu, P., Guhne, O., Goebel, A., Chen, Y.-A., Peng, C.-Z., Chen, Z.-B., and Pan, J.-W. (2010). Experimental demonstration of a hyper-entangled ten-qubit schrodinger cat state. *Nat. Phys.*, 6(5):331–335.

[67] Gedik, Z., Silva, I. A., Çakmak, B., Karpat, G., Vidoto, E. L. G., Soares-Pinto, D. O., DeAzevedo, E. R., and Fanchini, F. F. (2015). Computational speed-up with a single qudit. *Sci. Rep.*, 5(1):14671.

[68] Gisin, N. and Fröwis, F. (2018). From Quantum Foundations to Applications and Back. *ArXiv e-prints*.

[69] Gisin, N., Ribordy, G., Tittel, W., and Zbinden, H. (2002). Quantum cryptography. *Rev. Mod. Phys.*, 74(1):145–195.

[70] Gonçalves, D. S., Azevedo, C. L. N., Lavor, C., and Gomes-Ruggiero, M. A. (2018). Bayesian inference for quantum state tomography. *J. Appl. Stat.*, 45(10):1846–1871.

[71] Goyeneche, D., Cañas, G., Etcheverry, S., Gómez, E. S., Xavier, G. B., Lima, G., and Delgado, A. (2015). Five Measurement Bases Determine Pure Quantum States on Any Dimension. *Phys. Rev. Lett.*, 115(9):090401.

[72] Granade, C., Combes, J., and Cory, D. G. (2016). Practical Bayesian tomography. *New J. Phys.*, 18(3):033024.

[73] Grassl, M. and Scott, A. J. (2017). Fibonacci-lucas sic-povms. *J. Math. Phys.*, 58(122201).

[74] Gross, D., Liu, Y.-K., Flammia, S. T., Becker, S., and Eisert, J. (2010). Quantum State Tomography via Compressed Sensing. *Phys. Rev. Lett.*, 105(15):150401.

[75] Guérin, P. A., Feix, A., Araújo, M., and Brukner, C. (2016). Exponential communication complexity advantage from quantum superposition of the direction of communication. *Phys. Rev. Lett.*, 117:100502.

[76] Hameedi, A., Saha, D., Mironowicz, P., Pawłowski, M., and Bourennane, M. (2017). Complementarity between entanglement-assisted and quantum distributed random access code. *Phys. Rev. A*, 95:052345.

[77] Hardy, L. and van Dam, W. (1999). Quantum whispers. *Phys. Rev. A*, 59:2635.

[78] Hendrych, M., Gallego, R., Micuda, M., Brunner, N., Acin, A., and Torres, J. P. (2012). Experimental estimation of the dimension of classical and quantum systems. *Nat. Phys.*, 8(8):588–591.

[79] Holevo, A. S. (1973). Bounds for the quantity of information transmitted by a quantum communication channel. *Problems of Information Transmission*, 9:177.

[80] Hou, Z., Zhu, H., Xiang, G., Li, C., , and Guo, G. (2016). *NPJ Quantum Inf.*, 2(16001).

[81] Hradil, Z. (1997). Quantum-state estimation. *Phys. Rev. A*, 55(3):R1561–R1564.

[82] Huszár, F. and Houlsby, N. M. T. (2012). Adaptive Bayesian quantum tomography. *Phys. Rev. A*, 85(5):052120.

[83] Jack, B., Leach, J., Ritsch, H., Barnett, S. M., Padgett, M. J., and Franke-Arnold, S. (2009). Precise quantum tomography of photon pairs with entangled orbital angular momentum. *New J. Phys.*, 11(10):103024.

[84] James, D., Kwiat, P., Hradil, Z., Rehacek, J., and White, A. (2001a). Quantum state reconstruction: a comparison of maximum likelihood and tomographic schemes. In *Tech. Dig. Summ. Pap. Present. Quantum Electron. Laser Sci. Conf. Postconf. Tech. Dig. (IEEE Cat. No.01CH37172)*, volume 728, page 238. Opt. Soc. America.

[85] James, D. F. V., Kwiat, P. G., Munro, W. J., and White, A. G. (2001b). Measurement of qubits. *Phys. Rev. A*, 64(5):052312.

[86] Jones, K. (1991). Principles of quantum inference. *Ann. Phys. (N. Y).*, 207(1):140–170.

[87] Kaszlikowski, D., Gnaciński, P., Zukowski, M., Miklaszewski, W., and Zeilinger, A. (2000). Violations of local realism by two entangled N-dimensional systems are stronger than for two qubits. *Phys. Rev. Lett.*, 85(21):4418–4421.

[88] Kaznady, M. S. and James, D. F. V. (2009). *Phys. Rev. A*, 79(022109).

[89] Kochen, S. and Specker, E. P. (1975). The Problem of Hidden Variables in Quantum Mechanics. In *Logico-Algebraic Approach to Quantum Mech.*, pages 293–328. Springer Netherlands, Dordrecht.

[90] Kravtsov, K. S., Straupe, S. S., Radchenko, I. V., Houlsby, N. M. T., Huszár, F., and Kulik, S. P. (2013). Experimental adaptive Bayesian tomography. *Phys. Rev. A*, 87(6):062122.

[91] Krenn, M., Huber, M., Fickler, R., Lapkiewicz, R., Ramelow, S., and Zeilinger, A. (2014). Generation and confirmation of a (100 100)-dimensional entangled quantum system. *Proceedings of the National Academy of Sciences*, 111(17):6243–6247.

[92] Kues, M., Reimer, C., Roztocki, P., Cortés, L. R., Sciara, S., Wetzel, B., Zhang, Y., Cino, A., Chu, S. T., Little, B. E., Moss, D. J., Caspani, L., Azaña, J., and Morandotti, R. (2017). On-chip generation of high-dimensional entangled quantum states and their coherent control. *Nature*, 546(7660):622–626.

[93] Kushilevitz, E. and Nisan, N. (1997). *Communication complexity*. Cambridge University Press.

[94] Ladd, T. D., Jelezko, F., Laflamme, R., Nakamura, Y., Monroe, C., and O'Brien, J. L. (2010). Quantum computers. *Nature*, 464(7285):45–53.

[95] Landauer, R. (1996). The physical nature of information. *Phys. Lett. A*, 217:188.

[96] Langford, N. K., Dalton, R. B., Harvey, M. D., O'Brien, J. L., Pryde, G. J., Gilchrist, A., Bartlett, S. D., and White, A. G. (2004). Measuring Entangled Qutrits and Their Use for Quantum Bit Commitment. *Phys. Rev. Lett.*, 93(5):053601.

[97] Lanyon, B. P., Barbieri, M., Almeida, M. P., Jennewein, T., Ralph, T. C., Resch, K. J., Pryde, G. J., O'Brien, J. L., Gilchrist, A., and White, A. G. (2009). Simplifying quantum logic using higher-dimensional Hilbert spaces. *Nat. Phys.*, 5(2):134–140.

[98] Law, C. K., Walmsley, I. A., and Eberly, J. H. (2000). Continuous frequency entanglement: Effective finite hilbert space and entropy control. *Phys. Rev. Lett.*, 84(23):5304–5307.

[99] Lima, G., Gómez, E. S., Vargas, A., Vianna, R. O., and Saavedra, C. (2010). Fast entanglement detection for unknown states of two spatial qutrits. *Phys. Rev. A*, 82:012302.

[100] Lima, G., Neves, L., Guzmán, R., Gómez, E. S., Nogueira, W. A. T., Delgado, A., Vargas, A., and Saavedra, C. (2011). Experimental quantum tomography of photonic qudits via mutually unbiased basis. *Opt. Express*, 19(4):3542.

[101] Lima, G., Vargas, A., Neves, L., Guzmán, R., and Saavedra, C. (2009). Manipulating spatial qudit states with programmable optical devices. *Opt. Express*, 17(13):10688.

[102] Lo, H.-P., Li, C.-M., Yabushita, A., Chen, Y.-N., Luo, C.-W., and Kobayashi, T. (2016). Experimental violation of bell inequalities for multi-dimensional systems, sci. *Rep.*, 6:22088.

[103] Luo, M.-X., Chen, X.-B., Yang, Y.-X., and Wang, X. (2014). Geometry of Quantum Computation with Qudits. *Sci. Rep.*, 4(1):4044.

[104] Luo, S. (2008). Quantum discord for two-qubit systems. *Phys. Rev. A*, 77:042303.

[105] Mafu, M., Dudley, A., Goyal, S., Giovannini, D., McLaren, M., Padgett, M. J., Konrad, T., Petruccione, F., Lutkenhaus, N., and Forbes, A. (2013). Higher-dimensional orbital-angular-momentum-based quantum key distribution with mutually unbiased bases. *Phys. Rev. A*, 88:032305.

[106] Mahler, D. H., Rozema, L. A., Darabi, A., Ferrie, C., Blume-Kohout, R., and Steinberg, A. M. (2013). *Phys. Rev. Lett.*, 111(183601).

[107] Mair, A., Vaziri, A., Weihs, G., and Zeilinger, A. (2001). Entanglement of the orbital angular momentum states of photons. *Nature*, 412(6844):313–316.

[108] Malik, M., Erhard, M., Huber, M., Krenn, M., Fickler, R., and Zeilinger, A. (2016). Multi-photon entanglement in high dimensions. *Nat. Photon.*, 10(4):248–252.

[109] Marques, B., Matoso, A. A., Pimenta, W. M., Gutiérrez-Esparza, A. J., Santos, M. F., and Pádua, S. (2017). Experimental simulation of decoherence in photonics qudits. *Scientific Reports*, 5(16049).

[110] Martínez, D., Solís-Prosser, M. A., Cañas, G., Jiménez, O., Delgado, A., and Lima, G. (2019). Experimental quantum tomography assisted by multiply symmetric states in higher dimensions. *Phys. Rev. A*, 99(012336).

[111] Martínez, D., Tavakoli, A., Casanova, M., Cañas, G., Marques, B., and Lima, G. (2018). High-Dimensional Quantum Communication Complexity beyond Strategies Based on Bell's Theorem. *Phys. Rev. Lett.*, 121(15):150504.

[112] Masanes, L. (2002). Tight bell inequality for d-outcome measurements correlations. *Quantum Information and Computation*, 3:345.

[113] Mirhosseini, M., Magana-Loaiza, O. S., O'Sullivan, M. N., Rodenburg, B., Malik, M., Lavery, M. P. J., Padgett, M. J., Gauthier, D. J., and Boyd, R. W. (2015).

High-dimensional quantum cryptography with twisted light. *New J. Phys.*, 17:033033.

[114] Mohseni, M., Rezakhani, A. T., and Lidar, D. A. (2008). Quantum-process tomography: Resource analysis of different strategies. *Phys. Rev. A*, 77(3):032322.

[115] Monz, T., Schindler, P., Barreiro, J. T., Chwalla, M., Nigg, D., Coish, W. A., Harlander, M., Hänsel, W., Hennrich, M., and Blatt, R. (2011). 14-qubit entanglement: Creation and coherence. *Phys. Rev. Lett.*, 106:130506.

[116] Moreno, I., Velásquez, P., Fernández-Pousa, C. R., Sánchez-Lóez, M. M., Mateos, F., Sánchez-López, M. M., and Mateos, F. (2003). Jones matrix method for predicting and optimizing the optical modulation properties of a liquid-crystal display. *J. Appl. Phys.*, 94(6):3697–3702.

[117] Navascués, M. and Vértesi, T. (2015). Bounding the set of finite dimensional quantum correlations. *Phys. Rev. Lett.*, 115:020501.

[118] Navascués, M. and Wunderlich, H. (2009). A glance beyond the quantum model. *Proc. R. Soc. Lond. A*, 466:881890.

[119] Nayak, A. (1999). Optimal lower bounds for quantum automata and random access codes. In *Proceedings of the 40th IEEE Symposium on Foundations of Computer Science (FOCS'99)*, pages 369–376.

[120] Neves, L., Lima, G., Aguirre Gómez, J. G., Monken, C. H., Saavedra, C., and Pádua, S. (2005). Generation of Entangled States of Qudits using Twin Photons. *Phys. Rev. Lett.*, 94(10):100501.

[121] Neves, L., Pádua, S., and Saavedra, C. (2004). Controlled generation of maximally entangled qudits using twin photons. *Phys. Rev. A*, 69(4):042305.

[122] Nikolopoulos, G. M., Ranade, K. S., and Alber, G. (2006). Error tolerance of two-basis quantum-key-distribution protocols using qudits and two-way classical communication. *Phys. Rev. A*, 73(3):032325.

[123] O'Leary, D. P., Brennen, G. K., and Bullock, S. S. (2006). Parallelism for quantum computation with qudits. *Phys. Rev. A*, 74(3):032334.

[124] Ourjoumtsev, A., Jeong, H., Tualle-Brouri, R., and Grangier, P. (2007). Generation of optical Schrödinger cats' from photon number states. *Nature*, 448(7155):784–786.

[125] Paiva-Sánchez, C., Burgos-Inostroza, E., Jiménez, O., and Delgado, A. (2010). Quantum tomography via equidistant states. *Phys. Rev. A*, 82(3):032115.

[126] Pál, K. F. and Vértesi, T. (2009). Quantum bounds on bell inequalities. *Phys. Rev. A*, 79:022120.

[127] Pál, K. F. and Vértesi, T. (2010). Maximal violation of a bipartite three-setting, two-outcome bell inequality using infinite-dimensional quantum systems. *Phys. Rev. A*, 82:022116.

[128] Paris, M. and Reháček, J. (2004). *Quantum State Estimation*, volume 649 of *Lecture Notes in Physics*. Springer Berlin Heidelberg, Berlin, Heidelberg.

[129] Pawłowski, M. and Brunner, N. (2011). Semi-device-independent security of one-way quantum key distribution. *Phys. Rev. A*, 84:010302(R).

[130] Pawłowski, M., Paterek, T., Kaszlikowski, D., Scarani, V., Winter, A., , and Żukowski, M. (2009). *Information Causality as a Physical Principle, Nature*, 461:1101.

[131] Pawłowski, M. and Winter, A. (2012). Hyperbits: the information quasiparticles. *Phys. Rev. A*, 85:022331.

[132] Pawłowski, M. and Żukowski, M. (2010). Entanglement-assisted random access codes. *Phys. Rev. A*, 81:042326.

[133] Pears Stefano, Q., Rebón, L., Ledesma, S., and Iemmi, C. (2017). Determination of any pure spatial qudits from a minimum number of measurements by phase-stepping interferometry. *Phys. Rev. A*, 96(6):062328.

[134] Penrose, R. and Todd, J. A. (1955). A generalized inverse for matrices. *Math. Proc. Cambridge Philos. Soc.*, 51(03):406.

[135] Pereira, L., Martínez, D., Cañas, G., Lima, G., and Delgado, A. *in preparation*.

[136] Pereira, L., Zambrano, L., Cortés-Vega, J., Niklitschek, S., and Delgado, A. (2018). Adaptive quantum tomography in high dimensions. *Phys. Rev. A*, 98(1):012339.

[137] Pimenta, W. M., Marques, B., Carvalho, M. A., Barros, M. R., Fonseca, J. G., Ferraz, J., Terra Cunha, M., and Pádua, S. (2010). Minimal state tomography of spatial qubits using a spatial light modulator. *Opt. Express*, 18(24):24423.

[138] Pimenta, W. M., Marques, B., Maciel, T. O., Vianna, R. O., Delgado, A., Saavedra, C., and Pádua, S. (2013). Minimum tomography of two entangled qutrits using local measurements of one-qutrit symmetric informationally complete positive operator-valued measure. *Phys. Rev. A*, 88(1):012112.

[139] Press, W. H., Teukolski, S. A., Vetterling, W. T., and Flannery, B. P. (1992). *Numerical Recipes*. Cambridge University Press, Cambridge.

[140] Reháček, J., Hradil, Z., and Ježek, M. (2001). Iterative algorithm for reconstruction of entangled states. *Phys. Rev. A*, 63(4):040303.

[141] Renes, J. M., Blume-Kohout, R., Scott, A. J., and Caves, C. M. (2004). Symmetric informationally complete quantum measurements. *J. Math. Phys.*, 45(6):2171.

[142] Rossi, A., Vallone, G., Chiuri, A., De Martini, F., and Mataloni, P. (2009). Multipath Entanglement of Two Photons. *Phys. Rev. Lett.*, 102(15):153902.

[143] S. Muhammad, A. Tavakoli, M. K. M. P. M. Z. and Bourennane, M. (2014). Quantum bidding in bridge. *Phys. Rev. X*, 4:021047.

[144] Schack, R., Brun, T. A., and Caves, C. M. (2001). Quantum Bayes rule. *Phys. Rev. A*, 64(1):014305.

[145] Schwemmer, C., Knips, L., Richart, D., Weinfurter, H., Moroder, T., Kleinmann, M., and Gühne, O. (2015). Systematic Errors in Current Quantum State Tomography Tools. *Phys. Rev. Lett.*, 114(8):080403.

[146] Scott, A. J. and Grassl, M. (2010). Symmetric informationally complete positive-operator-valued measures: A new computer study. *J. Math. Phys.*, 51(042203).

[147] Shang, J., Zhang, Z., and Ng, H. K. (2017). Superfast maximum-likelihood reconstruction for quantum tomography. *Phys. Rev. A*, 95(6):062336.

[148] Silva, G. B., Glancy, S., and Vasconcelos, H. M. (2017). *Phys. Rev. A*, 95(022107).

[149] Slater, P. B. (1995). Quantum coin-tossing in a Bayesian Jeffreys framework. *Phys. Lett. A*, 206(1-2):66–72.

[150] Smania, M., Elhassan, A. M., Tavakoli, A., and Bourennane, M. (2016). Experimental quantum multiparty communication protocols. *npj Quantum Information*, 2:16010.

[151] Smolin, J. A., Gambetta, J. M., and Smith, G. (2012). *Phys. Rev. Lett.*, 108(070502).

[152] Solís-Prosser, M. A., Fernandes, M. F., Jiménez, O., Delgado, A., and Neves, L. (2017). Experimental Minimum-Error Quantum-State Discrimination in High Dimensions. *Phys. Rev. Lett.*, 118(10):100501.

[153] Solís-Prosser, M. A., Jiménez, O., Neves, L., and Delgado, A. (2013). Quantum teleportation via quantum channels with non-maximal Schmidt rank. *Phys. Scr.*, T153(T153):014058.

[154] Specker, E. (1960). Die Logik nicht gleichzeitig entscheidbarer Aussagen. *Dialectica*, 14(2-3):239–246.

[155] Stefano, Q. P., Rebón, L., Ledesma, S., and Iemmi, C. (2017). Determination of any pure spatial qudits from a minimum number of measurements by phase-stepping interferometry. *Phys. Rev. A*, 96:062328.

[156] Struchalin, G. I., Pogorelov, I. A., Straupe, S. S., Kravtsov, K. S., Radchenko, I. V., and Kulik, S. P. (2016). Experimental adaptive quantum tomography of two-qubit states. *Phys. Rev. A*, 93(1):012103.

[157] Taguchi, G., Dougakiuchi, T., Yoshimoto, N., Kasai, K., Iinuma, M., Hofmann, H. F., and Kadoya, Y. (2008). Measurement and control of spatial qubits generated by passing photons through double slits. *Phys. Rev. A*, 78(1):012307.

[158] Takesue, H. and Noguchi, Y. (2009). Implementation of quantum state tomography for time-bin entangled photon pairs. *Opt. Express*, 17(13):10976.

[159] Tavakoli, A., Hameedi, A., Marques, B., and Bourennane, M. (2015). Quantum random access codes using single d-level systems. *Phys. Rev. Lett.*, 114:170502.

[160] Tavakoli, A., Marques, B., Pawłowski, M., and Bourennane, M. (2016). Spatial versus sequential correlations for random access coding. *Phys. Rev. A*, 93:032336.

[161] Tavakoli, A., Pawlowski, M., Zukowski, M., and Bourennane, M. (2017). Dimensional discontinuity in quantum communication complexity at dimension seven. *Phys. Rev. A*, 95:020302.

[162] Tavakoli, A., Rosset, D., and Renou, M.-O. *Efficiently bounding finite-dimensional quantum correlations via symmetrisation*. In preparation.

[163] Tavakoli, A. and Żukowski, M. (2017). Higher-dimensional communication complexity problems: Classical protocols versus quantum ones based on bell's theorem or prepare-transmit-measure schemes. *Phys. Rev. A.*, 95:042305.

[164] Thew, R. T., Acín, A., Zbinden, H., and Gisin, N. (2004). Bell-type test of energy-time entangled qutrits. *Phys. Rev. Lett.*, 93:010503.

[165] Thew, R. T., Nemoto, K., White, A. G., and Munro, W. J. (2002). Qudit quantum-state tomography. *Phys. Rev. A*, 66(1):012303.

[166] Titchener, J. G., Gräfe, M., Heilmann, R., Solntsev, A. S., Szameit, A., and Sukhorukov, A. A. (2018). Scalable on-chip quantum state tomography. *npj Quantum Inf.*, 4(1):19.

[167] Tonchev, H. S. and Vitanov, N. V. (2016). Quantum phase estimation and quantum counting with qudits. *Phys. Rev. A*, 94(4):042307.

[168] Torres-Ruiz, F. A., Lima, G., Delgado, A., Pádua, S., and Saavedra, C. (2010). Decoherence in a double-slit quantum eraser. *Phys. Rev. A*, 81(4):042104.

[169] Trojek, P., Schmid, C., M. Bourennane, C. Brukner, M. Z., and Weinfurter, H. (2005). Experimental quantum communication complexity. *Phys. Rev. A*, 72:050305(R).

[170] Vandenberghe, L. and Boyd, S. (1996). Semidefinite programming. *SIAM Rev*, 38:49.

[171] Varga, J. J. M., Ledesma, S., Iemmi, C., and Rebón, L. (2017). Controlled generation of mixed spatial qudits with arbitrary degree of purity. *Phys. Rev. A*, 96(3):032309.

[172] Varga, J. J. M., Rebón, L., Solís-Prosser, M. A., Neves, L., Ledesma, S., and Iemmi, C. (2014). Optimized generation of spatial qudits by using a pure phase spatial light modulator. *J. Phys. B At. Mol. Opt. Phys.*, 47(22):225504.

[173] Vértesi, T., Pironio, S., and Brunner, N. (2010). Closing the Detection Loophole in Bell Experiments Using Qudits. *Phys. Rev. Lett.*, 104(6):060401.

[174] Wang, X.-L., Chen, L.-K., Li, W., Huang, H.-L., Liu, C., Chen, C., Luo, Y.-H., Su, Z.-E., Wu, D., Li, Z.-D., Lu, H., Hu, Y., Jiang, X., Peng, C.-Z., Li, L., Liu, N.-L., Chen, Y.-A., Lu, C.-Y., and Pan, J.-W. (2016). Experimental ten-photon entanglement. *Phys. Rev. Lett.*, 117:210502.

[175] Werner, R. F. and Wolf, M. M. (2001). Bell inequalities and entanglement. *Quantum Inf. Comput.*, 1:1.

[176] Wootters, W. K. and Fields, B. D. (1989). Optimal state-determination by mutually unbiased measurements. *Ann. Phys. (N. Y).*, 191(2):363–381.

[177] Yao, X.-C., Wang, T.-X., Xu, P., Lu, H., Pan, G.-S., Bao, X.-H., Peng, C.-Z., Lu, C.-Y., Chen, Y.-A., and Pan, J.-W. (2012). Observation of eight-photon entanglement. *Nat. Photon.*, 6(4):225–228.

[178] Yuan, Z.-S., Bao, X.-H., Lu, C.-Y., Zhang, J., Peng, C.-Z., and Pan, J.-W. (2010). Entangled photons and quantum communication. *Physics Reports*, 497(1):1 – 40.

[179] Zohren, S. and Gill, R. (2008). Maximal violation of the collins-gisin-linden-massar-popescu inequality for infinite dimensional states. *Phys. Rev. Lett.*, 100:120406.

[180] Żukowski, M., Zeilinger, A., Horne, M. A., and Weinfurter, H. (1998). Quest for GHZ States. *Acta Phys. Pol.*, 93(187).